

AKARI and Spinning Dust Emission
A look at microwave dust emission via the Infrared
Doctoral Thesis
DRAFT

Aaron Christopher Bell

December 6, 2017

Contents

2	1	Introduction	2
3	1.1	All-sky Astronomy	2
4	1.2	Infrared astronomy	2
5	1.3	Microwave foregrounds	5
6	1.3.1	Anomalous Microwave Emission	6
7	1.3.2	Proposed explanations	9
8	1.3.3	Excitation factors	11
9	1.3.4	AME vs. IR in the literature	12
10	1.4	Scope of this Dissertation	13
11	1.4.1	An application of all-sky archival data	13
12	1.4.2	Testing the spinning PAH hypothesis	13
13	1.4.3	Limitations	13
14	1.4.4	Code availability	14
15	2	Data Sources	15
16	2.1	A collection of skies	15
17	2.2	AKARI	16
18	2.2.1	AKARI/Infrared Camera (IRC)	16
19	2.2.2	The AKARI Far Infrared Surveyor (FIS)	20
20	2.2.3	Planck Observatory High Frequency Instrument (HFI)	20
21	2.3	Infrared Astronomical Satellite (IRAS)	21
22	2.4	Planck COMMANDER Parameter Maps	22
23	2.4.1	Synchrotron	22
24	2.4.2	Free-free emission	22
25	2.4.3	Thermal dust emission	24

26	2.4.4	AME data	24
27	2.5	All-sky Data Processing	29
28	3	Analysis of an interesting AME region: λ Orionis	31
29	3.1	An interesting AME region	31
30	3.1.1	Where does the ring come from?	31
31	3.1.2	A well-studied region	32
32	3.2	Investigative approach	32
33	3.3	Data preparation	35
34	3.3.1	Extraction from HEALPix maps	35
35	3.3.2	Point-source and artifact masking	35
36	3.3.3	PSF Smoothing	35
37	3.3.4	Background subtraction	36
38	3.4	Multi-wavelength characterization	36
39	3.4.1	Bootstrap analysis	37
40	3.5	Comparison with SED Fitting	39
41	3.6	Discussion	42
42	3.6.1	PAH Ionization fraction	44
43	4	All-sky Analysis	46
44	4.1	Resolution matching	46
45	4.2	All-sky cross correlations	47
46	4.3	Masked Comparison	49
47	4.3.1	Pixel mask	49
48	4.4	Spatial variation of correlations	53
49	4.5	Discussion	53
50	4.5.1	AME:Dust	53
51	4.5.2	AME:PAH	58
52	4.5.3	AME: T, G_0	58
53	4.5.4	Microwave foreground component separation	59

⁵⁴ List of Figures

55	1.1 An example of a potential makueup of microwave emission components. Photometry	
56	points are extracted from the Planck and WMAP all-sky maps (Planck Collaboration	
57	et al. 2014b), for a part of the region well-known for prominent AME, ρ Ophiuchus	
58	(Planck Collaboration et al. 2011b). The AME curve is produced from a warm neutral	
59	medium spinning dust template (Ali-Haïmoud et al. 2009), with a frequency-shift	
60	applied to approximately fit the microwave data s in Planck Collaboration et al. (2016b)	7
61	1.2 Two AME prominent regions investigated by Planck Collaboration et al. (2011b);	
62	Tibbs et al. (2011), ρ Ophiuchus and Perseus, as they appear in the PAH-feature-	
63	tracing AKARI/IRC $9\mu\text{m}$ all-sky data at native resolution (Ishihara et al. 2010). White	
64	contours show AME at 1-degree resolution, extracted from the map by Planck Col-	
65	laboration et al. (2016b). The IRC data shown here is of a much finer resolution than	
66	the AME data, at around $10''$, demonstrating the critical gap in resolvability of all-sky	
67	AME-tracing data itself vs. the IR dust tracers we hope to compare it to.	8
68	2.1 Relative spectral response curves of the bands used in this study. Expected dust emis-	
69	sion components, assuming the dust SED model by (Compiègne et al. 2011) are also	
70	shown. The components are summarized as emission from big grains (BGs, dashed	
71	yellow line), emission from very small grains (VSGs, dashed blue line), and emission	
72	from PAHs (dashed grey line).	16
73	2.2 The I12 (orange) and A9 (green) filters coverage of modeled ionized (PAH1, red) and	
74	neutral (PAH0, purple)components of PAH features by Compiègne et al. (2011). The	
75	difference in the PAH feature coverage mainly comes from the $6.2\ \mu\text{m}$ and $7.7\ \mu\text{m}$	
76	feature.	17

77	2.3	Coverage of MIR wavelengths by the filters used in this work. An Spitzer/IRS spec-		
78		trum (see AOT4119040) of the galactic plane (thin blue line) demonstrates how IRC		
79		and IRAS photometric bands trace these features on an all-sky basis (Ishihara et al.		
80		2007). Strong PAH features overlap with the A9 and I12, while the A18 and I25		
81		micron bands only trace much weaker features.	18	
82	2.4	Ionization fraction of PAHs vs. band ratios of I12, I25, W12, W25 vs. A9, for three		
83		ISRF strengths: Top: $G_0 = 100$, Middle: $G_0 = 1000$, and Bottom: $G_0 = 10000$.		
84		These ratios are determined by assuming the SED template of Compiègne et al. (2011)	19	
85	2.5	AKARI/IRC 9 μm to IRAS 12 μm intensity ratio.	20	
86	2.6	AKARI/IRC 9 μm to IRAS 25 μm intensity ratio.	21	
87	2.7	r_s cross correlation matrix of the PCCS maps: temperature T , emissivity index β , and		
88		amplitude at 545 GHz $I_{dust}(545)$ of thermal dust; intensity of free-free emission ff		
89		at ; intensity of synchrotron emisison at 4 MHz $Sync$; intensity of the AME var. freq.		
90		component AME at 22.8 GHz.	23	
91	2.8	The peak frequencies of the varying component AME_{var} . The pink shaded re-		
92		gion indicates frequencies not covered by either WMAP or Planck The green line		
93		at 33.5 GHz indicates the peak frequency of AME_{fix}	25	
94	2.9	Histograms of the peak intensity AME maps calculated from the original COMMANDER-		
95		AME reference frequency maps. The dominant component, AME_{var} is indicated in		
96		blue, for all pixels in the map, with their spinning dust intensities evaluated their peak		
97		frequencies (see Fig. 2.8.) AME_{fix} gives the peak intensity of the spatially-constant		
98		frequency component, indicating it is essentially always the weaker component. . . .	26	
99	2.10	All-sky map of the peak frequencies of the varying component AME_{var} , correspond-		
100		ing to Fig. 2.8. Virtually all of the purple regions of the map correspond to pixels		
101		flagged for point sources in the LFI data. There are very few notable structures in the		
102		frequency map overall, other than the galactic plane itself, ρ Ophiuchus, and Perseus.	27	
103	2.11	Spdust template spinning dust profiles fitted by PC15X when calculating AME_{var} .		
104		The reference frequency, 22.8 GHz is indicated by the vertical green line. Each tem-		
105		plate has the same AME_{var} amplitude of 100 μK , indicated by the horizontal green		
106		line, plotted to highlight the potential deviation between AME_{var} and the actual peak		
107		intensity.	28	

108	2.12 All-sky map of the ratio of two COMMANDER components- the frequency-varying	
109	AME component divided by the intensity of thermal dust emission at 545 GHz. There	
110	are some recognizable AME emission regions, such as λ Orionis. Large-scale patches	
111	of AME excess are noted to correspond to synchrotron emission (Hensley et al. 2016)	29
112	3.1 λ Orionis as it appears in the AKARI 9 μ m data. Contours indicate the AME, as given	
113	by the Planck PR2 AME map. The image is smoothed to a 1° PSF (much larger than	
114	the original 10 arcsec map). The λ Orionis star itself is approximately located at the	
115	center of the image.	33
116	3.2 λ Orionis as it appears in H-alpha emission by ?. Contours indicate AME emis-	
117	sion, from the variable frequency component. The colorbar indicates $H\alpha$ emission in	
118	Rayleighs. The field of view is slightly larger than that used for the IR comparison. .	34
119	3.3 A grid of thumbnails showing the λ Orionis region's structure, at 12 wavelengths,	
120	along with AME contours (shown in white countours. Spatial correlation seems to be	
121	the best at the shortest and longest wavelengths (AKARI/IRC 9 μ m and Planck/HFI	
122	550 μ m). The images are smoothed and interpolated for demonstration. Figure 3.1	
123	demonstrates the actual pixel grid used for the SED fitting and intensity correlation	
124	tests.	36
125	3.4 Intensity cross-correlation for all pixels in the λ Orionis cut-out region. r_s indicates	
126	the Spearman rank correlation coefficient for each plot.	37
127	3.5 r_s correlation matrix for all of the data used in the λ Orionis analysis.	38
128	3.6 Re-sampled (Bootstrap) correlation tests for IR emission in λ Orionis vs. AME, for	
129	both Spearman and Pearson correlation tests.)	40
130	3.7 Observed (black circles and errors) and synthetic photometry (gray dots) SED of a	
131	pixel within λ Orionis, along with the dust SED model fit results. Two SED fits are	
132	shown: on for the Bayesian fitting (magenta), and another showing the standard least-	
133	squares result for comparison (yellow). The fitted ISRF strength U , and fraction of	
134	mass in PAHs, q_{PAH} are also given.	41
135	3.8 The same as Fig. 3.7, but for a different pixel position. Corresponds to galactic coor-	
136	dinates...	41
137	3.9 Scatter plot with error elipses generated through the Bayesian SED fitting, of total	
138	dust mass M_{dust} vs. I_{AME} scaled by U	42

139	3.10	The same comparison is given by 3.9, but showing total mass of PAHs (M_{PAH}) rather than total dust mass on the y-axis.	43
140			
141	3.11	The same as in Figs. 3.9 and 3.10 , but specifically comparing an estimate of the ionized component of PAH mass.	43
142			
143	3.12	The Bayesian correlation probability distributions of Pearson's correlation coeffo- coemt (ρ) for the three physical parameters vs. the AME intensity: total dust mass, rho_{dust} (red); total PAH mass rho_{PAH} (green); and only the ionized PAH mass rho_{PAH+} (blue). Also given are the probabilities of either PAH component being better correlated with AME than dust mass, as well as the probability that ionized PAH mass correlates better than total PAH.	44
144			
145			
146			
147			
148			
149	4.1	Point-density distributions of the AME intensity (Y-axis) vs. the IR bands' intensities. Darker regions indicated higher pixel densities. Only a simple mask of pixels near the ecliptic plane has been applied.	47
150			
151			
152	4.2	ALL-SKY cross-correlation matrix for the 12 infrared bands sampled, as well as the PC component maps described in Ch. 2: the two AME components evaluated at their peak frequencies AME_{var} , AME_{fix} ; Syncrotron, and free-free), and ancilliary maps of N_H , H_α emission, and 408 MHz emission Haslam et al. (1982). The color-scale indicates (r_s). Results are based on the unmasked sky, but are split by Galactic latitude: pixels with $ \beta < 15deg$ (left) and $ \beta > 15deg$. The color and annotations indicate r_s as in Fig. 3.5.	48
153			
154			
155			
156			
157			
158			
159	4.3	All-sky map in A9 emission after applying the combined masks: ecliptic plane, galac- tic plane, point sources, and pixels with $S/N < 1$. This mask essentially outlines the galaxy, except for the most confused regions.	49
160			
161			
162	4.4	The same comparison as shown for Fig. 4.1, but with the mask applied as in Fig. 4.3.	50
163	4.5	Similar comparison to Fig. 4.1, with the IR intensities scaled by U for each pixel.	51
164	4.6	Cross-correlation (r_s matrix for the IR intensities (unscaled) vs. each other, esssen- tially the same comparison as in Fig. 4.2, except that the pixel mask is applied.	52
165			
166	4.7	Cross-correlation (r_s matrix for the U -normalized IR intensities vs. each other, and also against the AME components, other PC products, and ancilliary data. Only the IR maps are divided by U - other data is unchanged from Fig. 4.6	52
167			
168			
169	4.8	53

170	4.9	Spatial map of r_s between the AME and IR intensity for 4 bands: 9 μm , 12 μm , 25 μm , and 140 μm . r_s is calculated for all NSIDE 256 pixels within each NSIDE 8 pixel-sized bin.	54
173	4.10	54
174	4.11	55
175	4.12	55
176	4.13	Spatial map of r_s between the AME and IR intensity as in Fig. ??, but with the AME and IR maps first normalized by dust radiance R	56
178	4.14	56
179	4.15	57
180	4.16	57
181	17	Explained variance decline for principal component analysis performed on a set of 12 all-sky infrared maps. The first three components account for over 99% of the total variance. The PCA fit is performed on the whole sky, after whitening the data, using the “scikitlearn”	61
184			

¹⁸⁵

Chapter 1

¹⁸⁶

Introduction

¹⁸⁷

“It is now plain that about 75% of the data we would like to have can be obtained from good

¹⁸⁸

ground-based sites”

¹⁸⁹

-H. Johnson, 1966

¹⁹⁰

1.1 All-sky Astronomy

¹⁹¹

All-sky astronomy is not new. Indeed, the notion of capturing a particular “object” or “source” with a camera and saving it for later investigation would be completely alien to the first astronomers and astronavigators. Absence of telescopes forced us to describe the sky in terms of its larger patterns, brightest characters. What is new however is the notion of preparing an archive of the sky itself for not only the research whims of a single investigator, team, institute, or even a single nation rather, all-sky surveys tend to be international endeavors in their production, and even more so in their utilization.

¹⁹⁷

1.2 Infrared astronomy

¹⁹⁸

Infrared astronomy was essentially non-existent as recently as the 1920s, if we judge by the first IR observations (Pettit & Nicholson 1922, 1928). Mainstream IR astronomy is perhaps much younger, only really taking off — literally — in the post-war era, via balloon and rocket borne experiments (Johnson 1966). Compare this to visible wavelengths, a field so old we name it after the bio-evolutionary advent of sight, itself. Even radio astronomy with its own logistical and technological challenges, has been around since at least 1932.

²⁰⁴

Astronomers have not been content to be constrained by atmospheric IR windows, even from the

TABLE 1.1 Timeline of all-sky surveys

1983	IRAS	Neugebauer et al. (1984)
1989	COBE	Boggess et al. (1992)
1990	ROSAT	Truemper (1982)
2001	WMAP	Bennett et al. (2003b)
2003	2MASS	Skrutskie et al. (2006)
2003	GALEX	Martin et al. (2005)
2006	AKARI	Murakami et al. (2007)
2008	Fermi	Atwood et al. (2009)
2009	Planck	Planck Collaboration et al. (2011a)
2009	WISE	Wright et al. (2010)

205 best of ground-based sites. Or perhaps interests have shifted so dramatically since 1966, that all of
 206 the investigations enabled by rocket-based, space-based, even Boeing 747-based IR astronomy (e.g.
 207 SOFIA, the Stratospheric Observatory for Infrared Astronomy, Young et al. (2012)) would have bored
 208 75% of astronomers in the '60s. The meaning of "far infrared" has even redshifted, so to speak, from
 209 the Johnson (1966) definition of "4 to 22 um" — consider the "Far Infrared Surveyor" instrument
 210 onboard the AKARI satellite (Murakami et al. 2007), which observed from 50 to 180 μm (Kawada
 211 et al. 2007a)

212 For our purposes, we consider the FIR to cover 60 to 550 μm , partially out of convenience—
 213 FIR bands, in this paper, means the Infrared Astronomical Satellite (IRAS) 60 and 100 μm (Neuge-
 214 bauer et al. 1984), all four FIS bands, and the Planck Observatory's High Frequency Instrument
 215 (HFI) 857 GHz and 545 GHz bands (Planck Collaboration et al. 2011a, 2014b). The two AKARI
 216 Infrared Camera (IRC) (Onaka et al. 2007; Ishihara et al. 2010) bands and the IRAS 12 and 25 μm
 217 bands we will refer to collectively as the mid-infrared (MIR) bands.

218 The ability to map and archive the sky with satellites - not only in the optical and infrared, but
 219 well into the microwave regime — has enabled interdisciplinary research of the ISM. The merits
 220 of multiwavelength based investigations arise from the simple fact that the ISM is very complex—
 221 both in terms of the myriad forms of matter present, from plasmas to dust grains — and in countless
 222 physical processes at play. Consider the complex case of a supernova remnant influencing surrounding
 223 ISM: through a combined analysis of radio, mid-far infrared, and X-ray data, Lau et al. (2015) were
 224 able to characterize the history of dust production, heating, and destruction within the Sgr A East
 225 supernova remnant.

In the case of interstellar dust emission, especially, multi-wavelength analysis is crucial to understanding the individual components of interstellar dust emission. If we assume that grains in local thermal equilibrium emit in an essentially classical manner, we will quickly become frustrated by multi-band IR observations. It is believed that factors such as variations in the optical properties of dust grains leads to a deviation from blackbody emission. The intensity of such emission has come to be represented by a “modified blackbody” function, provided in Onaka et al. (1999) as follows:

$$I_d(\nu) \propto \nu^{\beta_d} B_\nu(T_d), \quad (1.2.1)$$

where β is known as the “emissivity index”, and T_d is the dust temperature. Tracing this emission from microwave to IR wavelengths, in the diffuse Milky Way, Planck Collaboration et al. (2016d) find a typical value of 1.6 ± 0.1 for β , and 19.4 ± 1.3 K for the dust temperature (assuming a single temperature component).

Even after adopting a modified blackbody, we will still be unable to explain dust emission if we include wavelengths from the mid to Far-IR. A modified blackbody underestimates dust emission on the Wiens side, such as that traced by IRAS, an effect first reported by Boulanger et al. (1985), and also found later in data collected by the Cosmic Background Explorer (COBE)’s Diffuse Infrared Background Experiment (Sodroski et al. 1987, 1994). This excess cannot be explained by temperature variations of grains large enough to be in thermal equilibrium, and likely comes from a smaller population of interstellar dust grains (Purcell 1976; Sellgren 1984; Dwek 1986; Draine & Li 2001a).

From the mid-to-near IR however, spectroscopic observations enabled and required the simple-two populations model of larger and smaller dust (e.g. Mathis et al. (1977)), to be expanded. “Unidentified IR bands” from 3 to $11 \mu\text{m}$ (hereafter, UIR bands), demonstrate another divergence from the canonical dust emission story. The UIR bands were first reported at 8 to $13 \mu\text{m}$ in planetary nebulae and Hii regions by Gillett et al. (1973, 1975) in ground-based observations. Observations by Merrill et al. (1975) noted another unexplained feature at $3.27 \mu\text{m}$, noting: “there are [...] similarities in the 8-13 μm spectra of NGC 253, NGC 7027, and BD +303639 Gillett et al. (1975)”. Features at 6.2 and $7.7 \mu\text{m}$ were reported by Russell et al. (1977) using the first airplane-mounted IR telescope and predecessor to SOFIA, the Kuiper Airborne Observatory. Sellgren et al. (1983) reported features at 3.3 and $3.4 \mu\text{m}$ being detected in reflection nebulae.

From this point, the UIR bands become much less of property of select objects in targeted observations, are seen observed throughout the Milky Way. Balloon-based observation by Giard et al. (1994)

confirmed that the $3.3 \mu\text{m}$ feature pervades throughout the Galactic plane. The first-ever airborne IR observatory, Kuiper Several years later, space-based spectroscopy with the Infrared Telescope in Space (IRTS)(Murakami et al. 1996) and Infrared Space Observatory (ISO)(Kessler et al. 1996) enabled confirmation by Onaka et al. (1996) and Mattila et al. (1996) that the mid-infrared UIR features are not limited to selection objects, but are present even in the diffuse galactic ISM by. Dwek et al. (1997) even reported that photometric excess in the COBE/DIRBE $12 \mu\text{m}$ band may be caused by the UIR bands, in and suggested they may be from these UIR features have come to be explained via polycyclic aromatic hydrocarbons (PAHs), a possibility which had been considered earlier by Al-lamandola et al. (1985); Puget et al. (1985). PAHs are a class of molecules composed primarily of fused carbon rings such as corannulene. PAHs and/or similar amalgams containing aromatic structures (e.g. quenched carbonaceous composites (QCCs), Sakata et al. (1984)) have been incorporated into dust mixture SED models over the last two decades (Draine & Li 2001b, 2007a; Hony et al. 2001; Compiègne et al. 2011; Galliano et al. 2011; Jones et al. 2013, 2017).

Moving in the opposite direction, into the Rayleigh-Jeans regime of thermal dust emission, multi-wavelength observations have opened up a new discipline: the disentanglement of interstellar dust emission from non-dust emission components. Most notably, separating fluctuations in the cosmic microwave background (CMB) from the microwave extent of thermal dust emission. Those studying the Milky Way itself, from the far IR into microwave and radio frequencies, are now collaborating closely with those interested in the precise nature of the CMB.

1.3 Microwave foregrounds

Much of the motivation between recent galactic microwave emission research has little to do with galactic ISM astronomy itself. Rather, our galaxy presents an inconvenience to observational cosmology in that it 'contaminates' observations of the CMB. The average SED of the CMB is simple enough to model, with a 2.755 K blackbody function. This temperature however means that the peak occurs between several microwave foreground components, from interstellar dust and gas, as displayed in Fig. 1.1. The difficulty of decomposing the microwave sky into galactic ISM, extragalactic, and CMB components has brought the detailed decomposition of the microwaveradio regime of ISM to the forefront of Planck Collaboration paper titles (Planck Collaboration et al. 2011a, 2014a, 2016a). Without extragalactic research, there would be no need for the word "foreground" in describ-

284 ing galactic microwave emission.

285 The ISM has intruded into cosmological studies perhaps most prominently with the first claimed
286 detection of B-mode polarization (Hanson et al. 2013; BICEP2 Collaboration et al. 2014; Flauger et al.
287 2014), and multiple response papers. The main consensus being that the validation of CMB-related
288 claims require a careful estimate of the contribution, in intensity and polarization, from interstellar
289 dust and the subsequent counterclaim that this detection arose from galactic dust(Planck Collabora-
290 tion et al. 2017; Sheehy & Slosar 2017). More recently AMI Consortium et al. (2012) had noted a
291 peculiar SunyaevZeldovich effect based galaxy cluster detection, AMI-CL J0300+2613. Perrott et al.
292 (2018) have since proposed that this may in fact arise from high galactic latitude dust via “anomalous
293 microwave emission” (AME).

294 1.3.1 Anomalous Microwave Emission

295 In our efforts to decompose and understand galactic microwave emission itself, there remains a con-
296 stant antagonist. Galactic foregrounds had been broken down into 3 dominant components: free-free
297 emission from ionized regions, synchrotron emission generated by electrons relativistically by the
298 Milky Way’s magnetic field, and the microwave extent of thermal dust emission (Bennett et al. 2003a;
299 Leach et al. 2008; Planck Collaboration et al. 2014c). Deviations from this understanding began to
300 appear in the early 1990s, with efforts by Kogut et al. (1996); Leitch et al. (1997) to carefully inves-
301 tigate the CMB. They had found a component of the microwave sky which implied unlikely spectral
302 indices for free-free or synchrotron emission. AME generally takes the form of an ’excess’ contin-
303 num emission source, having a peak somewhere between 10 to 40 GHz (see Fig. 1.1). This excess
304 defies predictions for known microwave emission mechanisms. AME still lacks a concrete physical
305 explanation. Also, the term itself can be a bit confusing, as the word “anomalous” tends to imply
306 localized outlier. The AME is shown to be more than an isolated anomaly, but an added component
307 of microwave emission appearing throughout the galaxy (de Oliveira-Costa et al. 1997; Bennett et al.
308 2003a; Dickinson et al. 2013). Fig 1.2 shows two prominent AME regions, ρ Ophiuchus and the Per-
309 sues Molecular Cloud investigated by Tibbs et al. (2011); Planck Collaboration et al. (2011b), as they
310 appear in AKARI/IRC $9\mu\text{m}$ all-sky map (Ishihara et al. 2010). In this section we will explain that
311 while there is indeed much mystery as to the exact mechanism(s) producing the AME, what causes its
312 spectral variations, and what might be its physical carrier(s) - it is by now, perhaps less than anom-
313 arious. Following subsections will discuss the history of AME and the produced physical explanations,

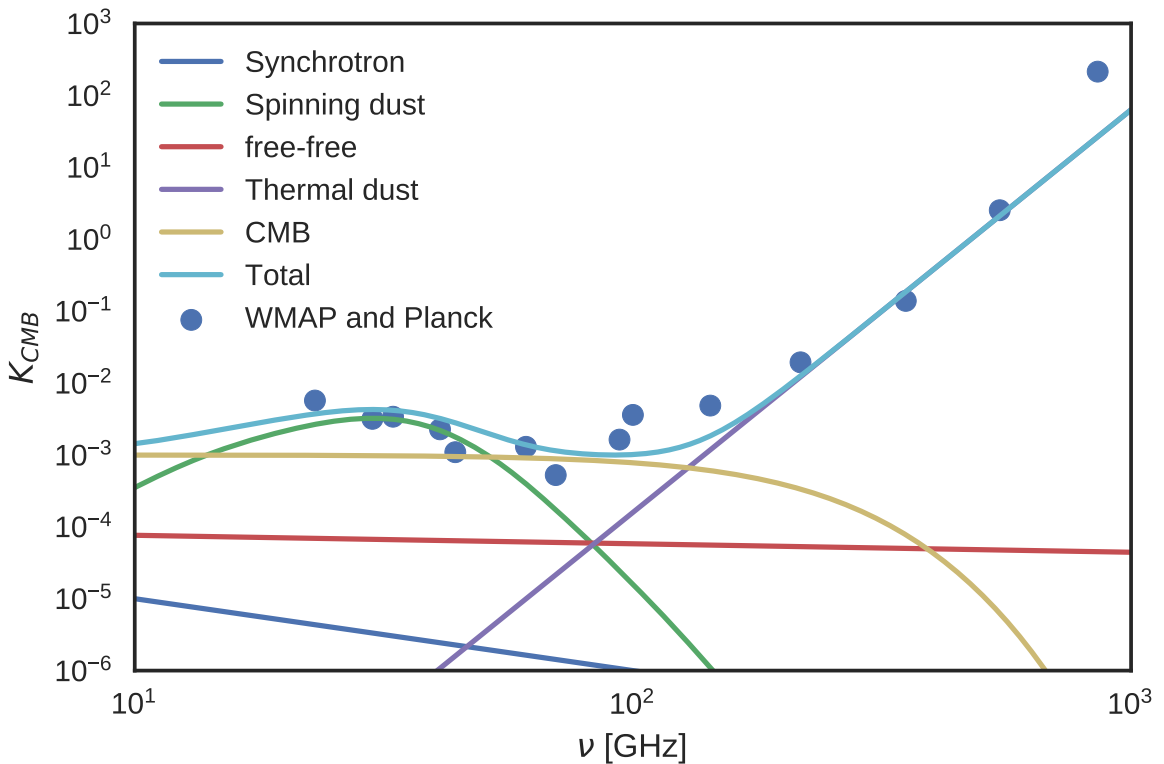


Figure 1.1: An example of a potential makueup of microwave emission components. Photometry points are extracted from the Planck and WMAP all-sky maps (Planck Collaboration et al. 2014b), for a part of the region well-known for prominent AME, ρ Ophiuchus (Planck Collaboration et al. 2011b). The AME curve is produced from a warm neutral medium spinning dust template (Ali-Haïmoud et al. 2009), with a frequency-shift applied to approximately fit the microwave data s in Planck Collaboration et al. (2016b)

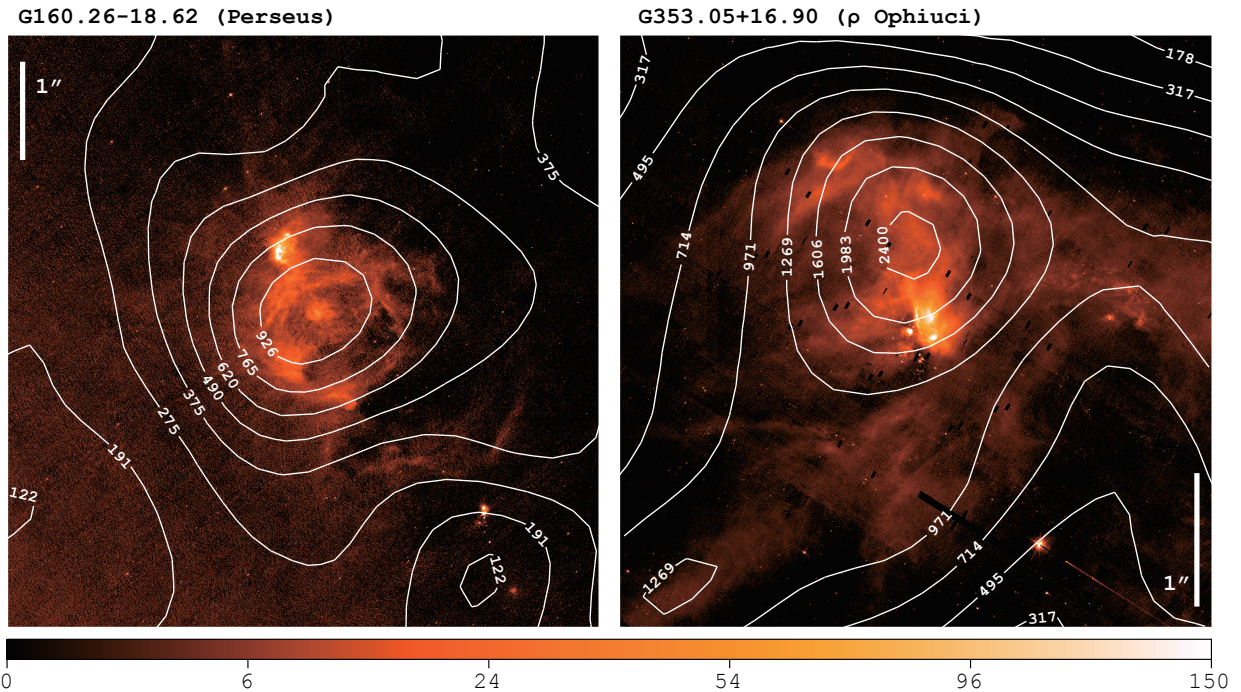


Figure 1.2: Two AME prominent regions investigated by Planck Collaboration et al. (2011b); Tibbs et al. (2011), ρ Ophiuchus and Perseus, as they appear in the PAH-feature-tracing AKARI/IRC $9\mu\text{m}$ all-sky data at native resolution (Ishihara et al. 2010). White contours show AME at 1-degree resolution, extracted from the map by Planck Collaboration et al. (2016b). The IRC data shown here is of a much finer resolution than the AME data, at around $10''$, demonstrating the critical gap in resolvability of all-sky AME-tracing data itself vs. the IR dust tracers we hope to compare it to.

314 as well comparisons between the AME and infrared emission from interstellar dust.

315 **Correlation with dust**

316 Since its first detection in early microwave observations, AME has been found to be a widespread
 317 feature of the microwave Milky Way (see the review Dickinson et al. (2013), and an updated state-
 318 of-play of AME research by Dickinson et al. (in prep). Kogut et al. (1996); de Oliveira-Costa et al.
 319 (1997) showed that the AME correlates very well with infrared emission from dust, via COBE/DIRBE
 320 and IRAS far-IR maps. Finkbeiner et al. (2002) reported the first detection of a “rising spectrum
 321 source at 8 to 10 GHz” in an observation targeting galactic ISM cloud. de Oliveira-Costa et al.
 322 (2002) further argued that this emission is in fact “ubiquitous”. The exact mechanism and carrier/s
 323 remain mysterious however. More recent works, employing observations by the Wilkinson Micrwave
 324 Anisotropy Probe (WMAP), Spitzer Space Telescope, the latest IR to microwave all-sky maps by
 325 Planck, and various ground based radio observations have strongly confirmed a relationship between
 326 interstellar dust emission and AME (Ysard & Verstraete 2010; Tibbs et al. 2011; Hensley et al. 2016).
 327 Exactly which physical mechanisms produces the AME however is still an open question, even if we
 328 assume a dusty AME origin. We equally puzzled as to the chemical composition and morphology of
 329 the carrier(s). We also lack an all-sky constraint on the emissivity of the AME spectrum at frequencies
 330 short of the WMAP cut-off, around 23 GHz. The typical peak frequency of AME, in those cases where
 331 it is constrained, does give us a clue.

332 **1.3.2 Proposed explanations**

333 From the observed spatial correlation between AME and dust emerged two prevailing hypotheses:
 334 1) Electric dipole emission by spinning small dust grains, a mechanism proposed in Erickson
 335 (1957) and Hoyle & Wickramasinghe (1970), with further discussion in Ferrara & Dettmar (1994).
 336 Draine & Lazarian (1998b) give the earliest thorough theoretical prediction of a spinning dust spec-
 337 trum. A decade later Ali-Haïmoud et al. (2009) contributed substantial updates, expanded modeling
 338 of grain excitation mechanisms and adoption of an updated grain size distribution by Weingartner
 339 & Draine (2001). Ysard & Verstraete (2010) introduced the first model of a spinning dust spectrum
 340 based on rotational emission from polycyclic aromatic hydrocarbons (PAHs), which are implicated
 341 due to their size. Draine & Lazarian (1998b), gives the expected rotational frequency of spinning dust

342 oscillators ω , as follows:

$$\frac{\omega_T}{2\pi} = \langle \nu^2 \rangle^{1/2} \approx 5.60 \times 10^9 a_{-7}^{-5/2} \xi^{-1/2} T_2^{1/2} \text{ Hz}, \quad (1.3.1)$$

343 where T is the gas temperature, a is the grain size, and ξ represents the deviation from a spherical
 344 moment of inertia. For example, we can take a typical peak frequency of the AME of 20 GHz, a gas
 345 temperature of 100 K, roughly spherical grains, and a dipole moment on the order of 1 debye, and
 346 get:

$$\frac{\omega_T}{2\pi} = 20 \text{ GHz} \left(\frac{T}{100 \text{ K}} \right)^{1/2} \left(\frac{\rho}{3 \text{ g cm}^{-3}} \right)^{-1/2} \left(\frac{a}{5 \text{ \AA}} \right)^{-5/2} \quad (1.3.2)$$

347 implying an oscillator size of approximately 1 nm. Thus PAHs, as considered by Ysard & Verstraete
 348 (2010), are a primary candidate spinning dust carrier, due to their expected size range.

349 2) Magnetic dipole emission, caused by thermal fluctuations in grains with magnetic inclusions,
 350 proposed by Draine & Lazarian (1999). More recently, modeled spectra for potential candidate carri-
 351 ers have appeared in the literature: PAHs, grains with magnetic inclusions (Draine & Hensley 2013;
 352 Ali-Haïmoud 2014; Hoang et al. 2016).

353 A third, but not widely accepted, possible explanation for AME is discussed in Jones (2009).
 354 They have suggested that the emissivity of dust, in the spectral range related to AME, could contain
 355 features caused by low temperature solid-state structural transitions.

356 Spinning dust

357 Spinning dust need not be the only emission mechanism, a convention as arisen in AME observational
 358 works. The photometric signature of the AME is frequently interpreted via spinning dust parameters
 359 (Ysard et al. 2011; Ali-Haimoud 2010). Archival all-sky AME data products exclusively assume
 360 a spinning dust SED templates. Both WMAP and Planck used a base template with 30 GHz peak
 361 frequency, and an assumed cold neutral medium environment. Using the “spdust” spinning dust SED
 362 model code to fit excess microwave foreground emission has become analogous fitting a modified
 363 blackbody function to the far IR.

364 We explore the case that the AME signature arises from spinning dust emission. If the AME
 365 is carried by spinning dust, the carrier should be small enough that it can be rotationally excited to
 366 frequencies in the range of 10-40 GHz, and must have a permanent electric dipole. Within contem-
 367 porary dust SED models, only the polycyclic aromatic hydrocarbon family of molecules (PAHs), or

368 nanoscale amorphous carbon dust fit these criteria. Those PAHs which have a permanent electric
 369 dipole (i.e. coranulene, but not symmetric molecules like coronene), can emit rotationally. How-
 370 ever the carrier need not be carbon-based. Indeed, Hensley & Draine (2017) claim that AME can be
 371 explained without carbonaceous carriers, using only spinning nanosilicates.

372 Spinning PAHs?

373 Assuming the rotational emission model of Draine & Lazarian (1998b), the AME signature (consis-
 374 tent with peaked, continuum emission having a peak between 15 and 50 GHz) implies very small
 375 oscillators (~ 1 s nm).

376 In any case, the PAH class of molecules are the only spinning dust candidate so far which show
 377 both:

- 378 1) Evidence of abundance in the ISM at IR wavelengths, and
- 379 2) A predicted range of dipole moments (on order of 1 debye), to produce the observed AME signature
- 380 (Draine & Lazarian 1998b; Lovas et al. 2005; Thorwirth et al. 2007).

381 However, it should be noted that although nanosilicates have not yet been detected in the ISM,
 382 Hensley & Draine (2017) propose that an upper bound on the abundance of nanosilicates by Li &
 383 Draine (2001) (based on IRTS observations by Onaka et al. (1996)), allow such small spinning grains
 384 to be composed primarily of silicates.

385 While neither nanosilicates nor any particular species of PAHs have been conclusively identified in
 386 the ISM, there is far more empirical evidence for PAH-like dust than for nanosilicates. Mid-infrared
 387 features associated with PAH-like aromatic materials have been observed. In fact, “the PAH features”
 388 are ubiquitous in the ISM (Giard et al. 1994; Onaka et al. 1996; Onaka 2000), such that the carriers
 389 must be abundant. Andrews et al. (2015) strongly argue for the existence of a dominant “grandPAH”
 390 class, containing 20 to 30 PAH species.

391 1.3.3 Excitation factors

392 In the spinning dust model, there are several possible excitation factors for spinning dust. For the
 393 grains to have rotational velocities high enough to create the observed AME, they must be subject
 394 to strong excitation mechanisms. The dominant factors that would be giving grains their spin, are
 395 broken down by Draine (2011) into basically two categories: 1) Collisional excitation. 2) Radiative
 396 excitation, the sum of which could lead to sufficient rotational velocities for sufficiently small grains.

397 However the extent of excitation will depend on environmental conditions, i.e. there will be more
 398 frequent encounters with ions and atoms in denser regions (so long as the density is not high enough
 399 to coagulate the small grains), and more excitation due to photon emission with increasing ISRF
 400 strength (Ali-Haïmoud et al. 2009; Ali-Haïmoud 2014). One of the strongest potential excitation
 401 mechanims listed in Draine (2011) is that of negatively charged grains interacting with ions. Thus
 402 not only must we consider environmental factors, grain composition and size, but also the ionization
 403 state of the carriers. (For example, ionized vs. neutral PAHs.) The dependence of the observed AME
 404 on ISM density is modeled by Ali-Haimoud (2010).

405 1.3.4 AME vs. IR in the literature

406 The overall pattern among large-scale studies seems to show that all of the dust-tracing photometric
 407 bands correlate with the AME (and each other) to first-order. On an all-sky, pixel-by-pixel basis,
 408 at 1° angular resolution, Ysard et al. (2010) find that $12\ \mu\text{m}$ emission, via IRAS, correlates slightly
 409 more strongly with AME (via WMAP) than with $100\ \mu\text{m}$ emission. They also find that scaling the IR
 410 intensity by the interstellar radiation field strength (given as G_0 , a measure of ISRF relative to that of
 411 the solar neighborhood) improves both correlations. They interpret this finding as evidence that AME
 412 is related to dust, and more closely related to the small stochastically emitting dust — predominantly
 413 PAHs — that is traced by $12\ \mu\text{m}$ emission. The improvement of the correlations after scaling by G_0
 414 is expected, as long as the $12\ \mu\text{m}$ or $9\ \mu\text{m}$ photometric bands are by stochastic emisson from PAHs,
 415 in other words:

$$I_{12\ \mu\text{m}} \propto G_0 N_{PAH}, \quad (1.3.3)$$

416 where N_{PAH} is the column density of emitting PAHs (Onaka 2000). Thus it implies that $I_{12\ \mu\text{m}}/G_0$
 417 is giving us a measure of the column density of spinning dust.

418 In a similar work however Hensley et al. (2016) report a lack of support for the spinning PAH
 419 hypothesis. Finding that fluctuations in the ratio of PAH-dominated $12\ \mu\text{m}$ emission (via WISE) to
 420 dust radiance, R , (via Planck) do not correlate with the ratio of AME intensity to R , they conclude
 421 that the AME is not likely to come from PAHs. In terms of emission intensity however, their findings
 422 are consistent with Ysard et al. (2010) in that $I_{12\ \mu\text{m}}$ correlates well with I_{AME} . Thus there remains
 423 an open question as to what the actual carrier of the AME is.

424 The story is no more clear when looking at the average properties of individual regions. Planck
 425 Collaboration et al. (2014d) find that among 22 high-confidence “AME regions” (galactic clouds

426 such as the ρ Ophiuchus cloud and the Perseus molecular cloud complex) AME vs. $12\ \mu\text{m}$ shows a
 427 marginally weaker correlation than AME vs. $100\ \mu\text{m}$ (via IRAS). Tibbs et al. (2011) examined the
 428 AME-prominent Perseus Molecular Cloud complex, finding that while there is no clear evidence of a
 429 PAH-AME correlation, they do find a slight correlation between AME and G_0 .

430 1.4 Scope of this Dissertation

431 We attempt to add to the understanding of AME and the possibility of spinning dust emission. With
 432 ample multiwavelength data now available, and a new PAH-focused all-sky survey in preparation by
 433 AKARI, we further test the PAH hypothesis, and assess how the IR to AME correlation changes as a
 434 function of wavelength.

435 1.4.1 An application of all-sky archival data

436 This is an astrophysical data archive based work. The primary goal is to highlight a particular ap-
 437 plication of multiwavelength (mid-IR to radio), cross-archive all-sky data analysis. We describe the
 438 interrelatedness between mid to far IR dust emission and possible microwave emission from dust.
 439 This is accomplished through an investigation of photometric all sky maps mainly from AKARI,
 440 IRAS, and Planck.

441 1.4.2 Testing the spinning PAH hypothesis

442 For the present work, we consider the spinning PAH hypothesis to have the highest degree of testa-
 443 bility, due to the well-established presence of aromatic emisison features in the ISM. We do not argue
 444 against the physical plausibility of nanosilicates to produce the AME. Indeed, there is no argument to
 445 date that these potential physicalities are mutually exclusive, as long as both potential carriers are suf-
 446 ficiently abundant. Nor does spinning dust emission theoretically exclude magnetic dipole emission
 447 or microwave thermal dust emissivity fluctuations.

448 1.4.3 Limitations

449 We do not explore the modeling of microwave dust emission itself, rather we refer to estimates of
 450 spinning dust emisison provided in the literature (Planck Collaboration et al. 2014c; Bennett et al.
 451 2003a) in the form of archival data and parameter maps. We consider this problem first on an all-sky

452 basis, not focusing on any pre-selected object of the sky — in order to assess if there any general
453 pattern between the IR and the AME, beyond the AME-dust correlation already described above. We
454 then focus on a region highlighted by the Planck Collaboration as being especially worthy of further
455 investigation (Planck Collaboration et al. 2016b), and has a resolvable topology even at 1-degree
456 resolution. Essentially all of the analyses and conclusions presented in this work apply to an angular
457 scale of approximately 1-degree, and only for the given component separation methods (Solar system,
458 galactic, extragalactic) used by each of the data providers.

459 **1.4.4 Code availability**

460 This dissertation is accompanied by a github repository.¹ Virtually all of the analyses code are avail-
461 able in that repository, in the form of Jupyter notebooks (along with the figures and the code used to
462 generate them.) The dust SED fitting code is not part of that repository, but is described in Galliano
463 et al. (in prep.)

¹Available at: <https://github.com/aaroncnb/CosmicDust>.

⁴⁶⁴ **Chapter 2**

⁴⁶⁵ **Data Sources**

⁴⁶⁶ **2.1 A collection of skies**

⁴⁶⁷ This work relies completely on all-sky surveys. All of the maps utilized are photometric-band infrared
⁴⁶⁸ maps, except for the AME data, which is an all-sky component separation analysis product, from the
⁴⁶⁹ Planck Collaboration's efforts to separate galactic foregrounds from the CMB. Table 2.1 summarizes
the observational data used in this thesis. In total, we employ all-sky maps from 12 photometric

Table 2.1: Observational data sources used in this article

Instrument	Central Wavelength	FWHM	Cali	Reference
AKARI/IRC	9 μm	~10"	<10%	¹
AKARI/IRC	18 μm	~10"	<10%	"
AKARI/FIS	65 μm	63"	<10%	²
AKARI/FIS	90 μm	78"	<10%	"
AKARI/FIS	140 μm	88"	<10%	"
AKARI/FIS	160 μm	88"	<10%	"
IRAS/IRIS	12 μm	4.0'	<5.1%	³
IRAS/IRIS	25 μm	4.0'	<15.1%	"
IRAS/IRIS	60 μm	4.2'	<10.4%	"
IRAS/IRIS	100 μm	4.5'	<13.5%	"
Planck/HFI	345 μm	4.7'		⁴
Planck/HFI	550 μm	4.3'		"

⁴⁷⁰

⁴⁷¹ bands, spanning the wavelength range of 6.9 μm to 550 μm as showin in Fig. 2.1 The following
⁴⁷² sections give the details of the observational data from each instrument as well as of the parameter

¹Ishihara et al. (2010)

²Doi et al. (2015); Takita et al. (2015)

³Miville-Deschénes & Lagache (2005)

⁴Planck Collaboration et al. (2014b)

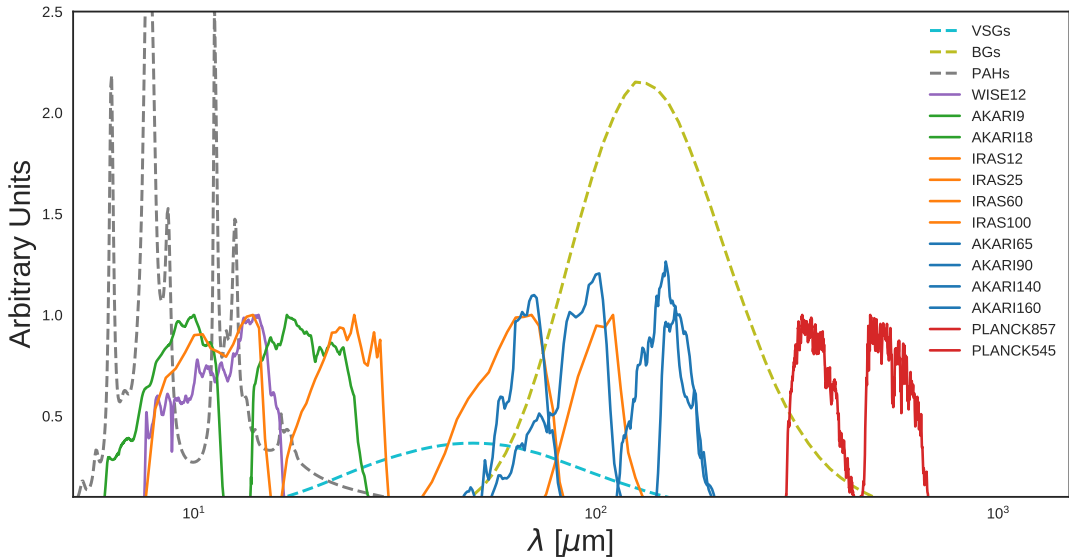


Figure 2.1: Relative spectral response curves of the bands used in this study. Expected dust emission components, assuming the dust SED model by (Compiègne et al. 2011) are also shown. The components are summarized as emission from big grains (BGs, dashed yellow line), emission from very small grains (VSGs, dashed blue line), and emission from PAHs (dashed grey line).

maps provided in Planck Collaboration et al. (2016b).⁵ From this point in the thesis, we will mostly use abbreviations to refer to the different bands, as follows: 'A' indicates AKARI; 'D', DIRBE; 'I', IRAS, and 'P' Planck. The number after each letter indicates the band central nominal wavelength in microns (or frequency in GHz, in the case of the Planck bands.)

2.2 AKARI

The AKARI infrared space telescope revealed an entire sky of infrared light, from the mid to far infrared, via two instruments (Murakami et al. 2007) the Infrared Camera (IRC)(Onaka et al. 2007) and the Far Infrared Surveyor (FIS) (Kawada et al. 2007b). In this section we will discuss the all-sky surveys produced by these two instruments.

2.2.1 AKARI/Infrared Camera (IRC)

IRC provided us with both spectroscopic and photometric data from the near to mid-infrared. In this work, we utilize the all-sky maps centered at 9 and 18 μm , created during by the IRC's fast-scanning mode. We utilize the most recent version of the IRC data (Ishihara, et al., in prep.) This version has

⁵Planck bands are named according to their central frequency, not wavelength.

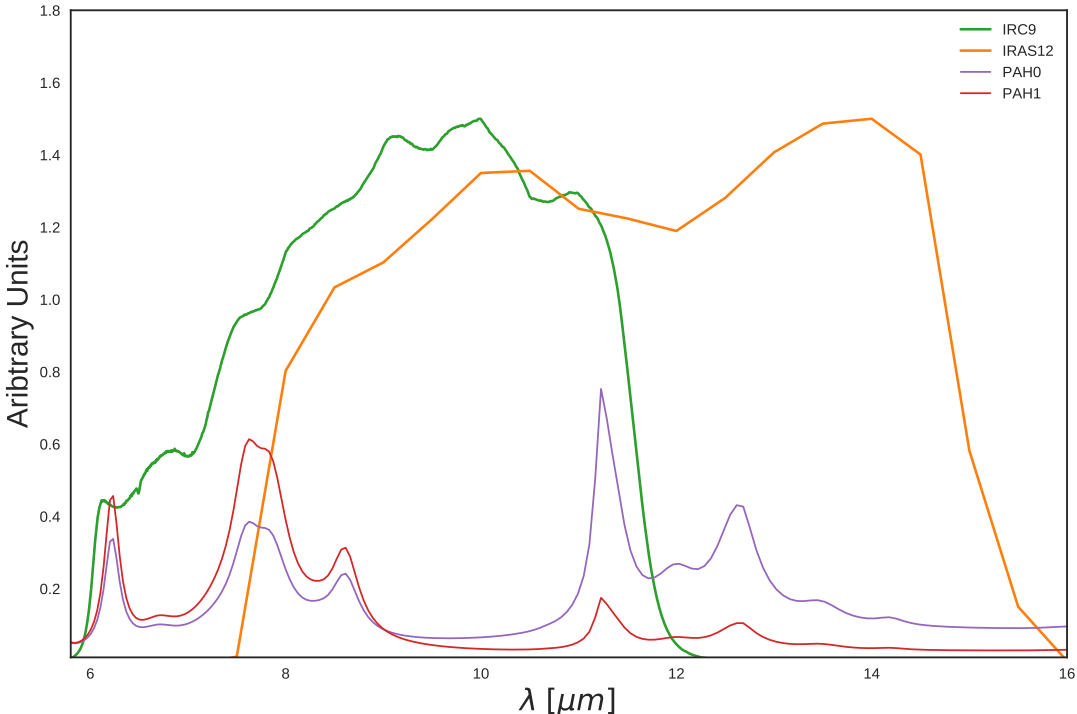


Figure 2.2: The I12 (orange) and A9 (green) filters coverage of modeled ionized (PAH1, red) and neutral (PAH0, purple) components of PAH features by Compiègne et al. (2011). The difference in the PAH feature coverage mainly comes from the $6.2 \mu\text{m}$ and $7.7 \mu\text{m}$ feature.

486 had an updated model of the Zodiacial light, fitted and subtracted. The details of the improved Zodi-
 487 model, which offers an improvement over that used for the IRAS all-sky maps, are given in Kondo
 488 et al. (2016).

489 PAH feature coverage

490 The A9 all-sky map demonstrates the abundance of the PAH bands carrier in the Milky Way (Ishihara
 491 et al. 2010). Figure 2.2 shows the coverage of the PAH features (from both ionized and neutral PAH
 492 components), as they are theoretically determined in Compiègne et al. (2011). The A9 band uniquely
 493 covers major ionized PAH features at $6.2 \mu\text{m}$ and $7.7 \mu\text{m}$; as well as neutral PAH features at $8.6 \mu\text{m}$ and
 494 $11.2 \mu\text{m}$ across the entire sky (Onaka et al. 2007). The I12 band covers the $11.2 \mu\text{m}$ and $8.6 \mu\text{m}$ features,
 495 and the similarly-shaped W12 band covers primarily the $11.2 \mu\text{m}$ feature but do not cover the $7.7 \mu\text{m}$
 496 completely. According to the distribution of PAH features across the response filters in Fig. 2.2, and
 497 referring back to the various dust components in Fig. 2.1 it is also expected that the A9 band is most
 498 dominated by PAH emission even with increasing G_0 . This may seem counter-intuitive, since, as
 499 described in Ch. 1, the PAH spectral shape does not show a temperature variation. However as T

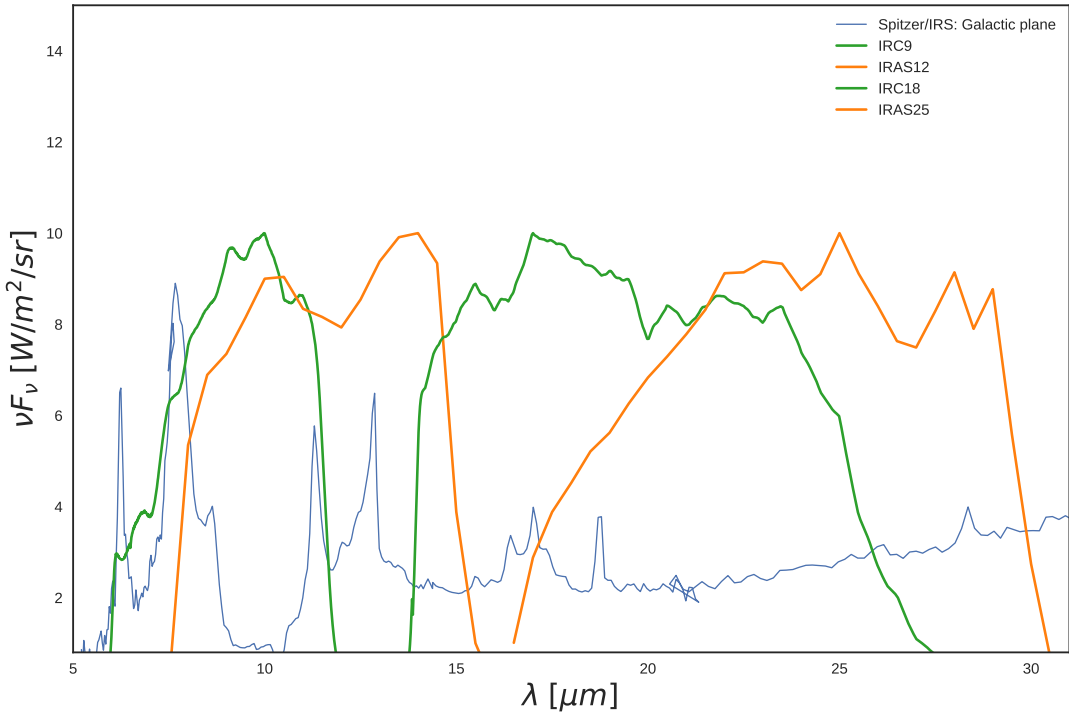


Figure 2.3: Coverage of MIR wavelengths by the filters used in this work. An Spitzer/IRS spectrum (see AOT4119040) of the galactic plane (thin blue line) demonstrates how IRC and IRAS photometric bands trace these features on an all-sky basis (Ishihara et al. 2007). Strong PAH features overlap with the A9 and I12, while the A18 and I25 micron bands only trace much weaker features.

increases, the MIR extent of thermal dust emission and emission from VSGs encroach on I12 and WI2 sooner than A9, diluting emission from PAHs. In some ionized regions, I12 may also include non-significant contributions from the NeII line at $12.8\text{ }\mu\text{m}$. Figure 2.3 demonstrates an example observational galactic cirrus spectrum in the MIR, from Spitzer Infrared Spectrograph (IRS) (Werner et al. 2004) data from), along with filters for all of the MIR bands used in this study. It indicates that the other MIR bands, A18 and I25, do cover strong PAH features and are expected to be dominated rather by emission from very small grains (VSGs), as was indicated in Fig. 2.1.

To help demonstrate how the relative contribution from PAHs will change for each band, for different ISRF strengths, Fig. ?? gives just such a calculation. These contributions remain relatively constant out to a G_0 of about 100, with the contribution from warm dust becoming a larger factor for the I12 and W12 bands. Thus, according to the DL01 template, A9 should have the highest contribution from PAHs out to extreme radiation fields. At least to the extent with which PAHs can endure harsh UV radiation, as PAHs are expected to be destroyed in some environments (Allain et al. 1996a,b; Pilleri et al. 2012; Pavlyuchenkov et al. 2013).

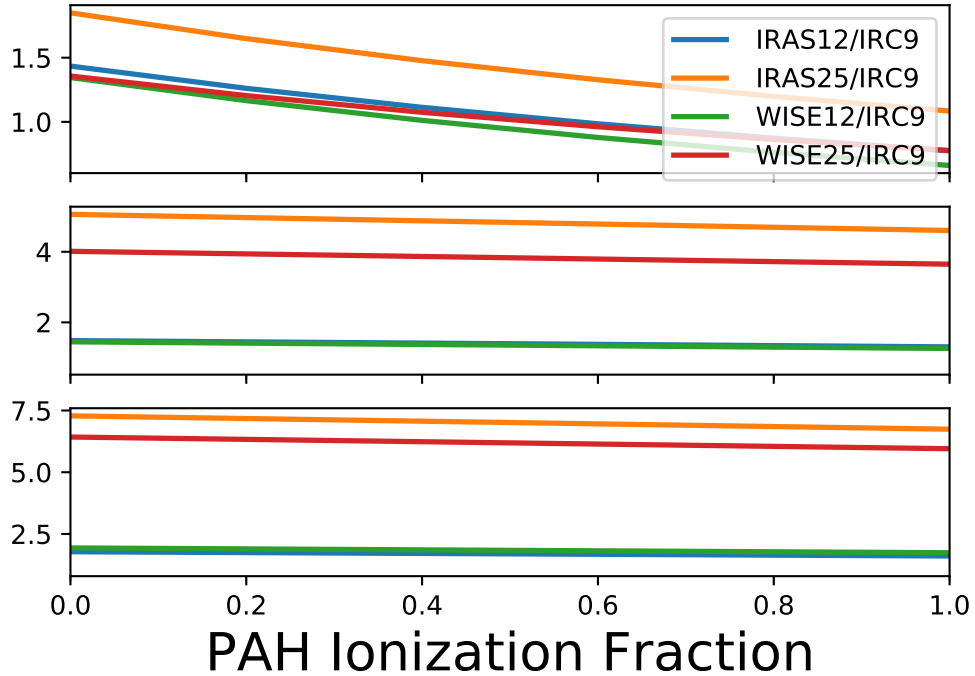


Figure 2.4: Ionization fraction of PAHs vs. band ratios of I12, I25, W12, W25 vs. A9, for three ISRF strengths: Top: $G_0 = 100$, Middle: $G_0 = 1000$, and Bottom: $G_0 = 10000$. These ratios are determined by assuming the SED template of Compiègne et al. (2011)

514 PAH ionization

515 Figure 2.2 indicates that expected emission from ionized PAHs will preferentially contribute to the A9
 516 band, even though both I12 and A9 cover ionized and neutral features. To estimate the extent to which
 517 the ionization fraction would effect the intensity ratio of these two bands, Fig. 2.4 gives the results of
 518 a calculation based on the Draine & Li (2001b) dust model, for various strengths of G_0 . demonstrates
 519 how the band ratios of the IRC μm band vs. the other MIR bands change with different modeled
 520 PAH ionization fractions (determined using the DustEM default model template, by Compiègne et al.
 521 (2011)). This band ratio can be determined, because the IRC9 filter is more sensitive to ionized PAH
 522 features, relative to IRAS12 or to WISE12.

523 IRC 9 μm shows a larger contribution from ionized PAHs and a conversely smaller contribution
 524 from neutral PAHs. Fig. 2.5 and Fig. 2.6 show the R(A9:I12) and R(A9:I25) ratio maps, demon-
 525 strating the relative variations in these MIR bands accross the sky- or at least the portions of the sky
 526 where S/N is sufficient. While from visual inspection the various MIR intensity all-sky maps appear
 527 to essentially trace the same stuctures of the galaxy, the ratio maps reveal that there are indeed dif-
 528 ferences to be explored. In regions where noise is dominant, ascertaining the ionization fraction will
 529 be quite difficult. This can be easily seen upon visual inspection of the ratio maps, in that there is

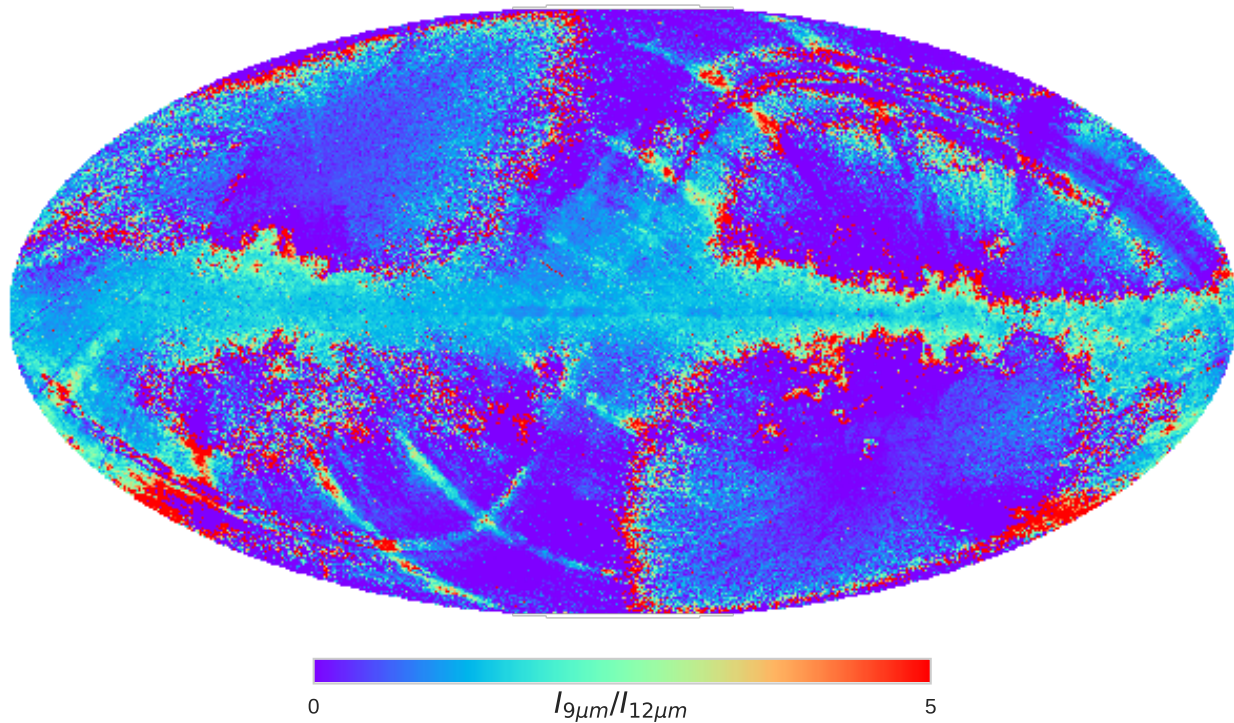


Figure 2.5: AKARI/IRC 9 μm to IRAS 12 μm intensity ratio.

530 a clear deliniation between brighter emission towards lower galactic latitudes, and the high latitude
 531 sky where the ratio shows very little discernible structure (except for the Zodi-residual patterns which
 532 differ between IRC and IRAS.) Thus even with the high latitude issues, there remains a large portion
 533 of the sky where a tracing of the ionization fraction may be feasible. This possibility is explored in
 534 Ch. 3, in looking at the PAH distribution within λ Orionis.

535 2.2.2 The AKARI Far Infrared Surveyor (FIS)

536 FIS gives us photometric data around the peak of the typical thermal dust SED. FIS was equipped
 537 with four wavebands: two narrow bands centered at 65 μm and at 160 μm , and two wide bands at
 538 90 μm and at 140 μm . An all-sky survey was carried out at each band (Kawada et al. 2007a), and the
 539 processed maps have been publicly released (Doi et al. 2015).

540 2.2.3 Planck Observatory High Frequency Instrument (HFI)

541 The HFI all-sky maps, spanning 100 to 857 GHz (Planck Collaboration et al. 2014b) help constrain
 542 the far IR dust emissivity. This study utilizes the 857 GHz (345 μm) and 545 GHz (550 μm) bands.

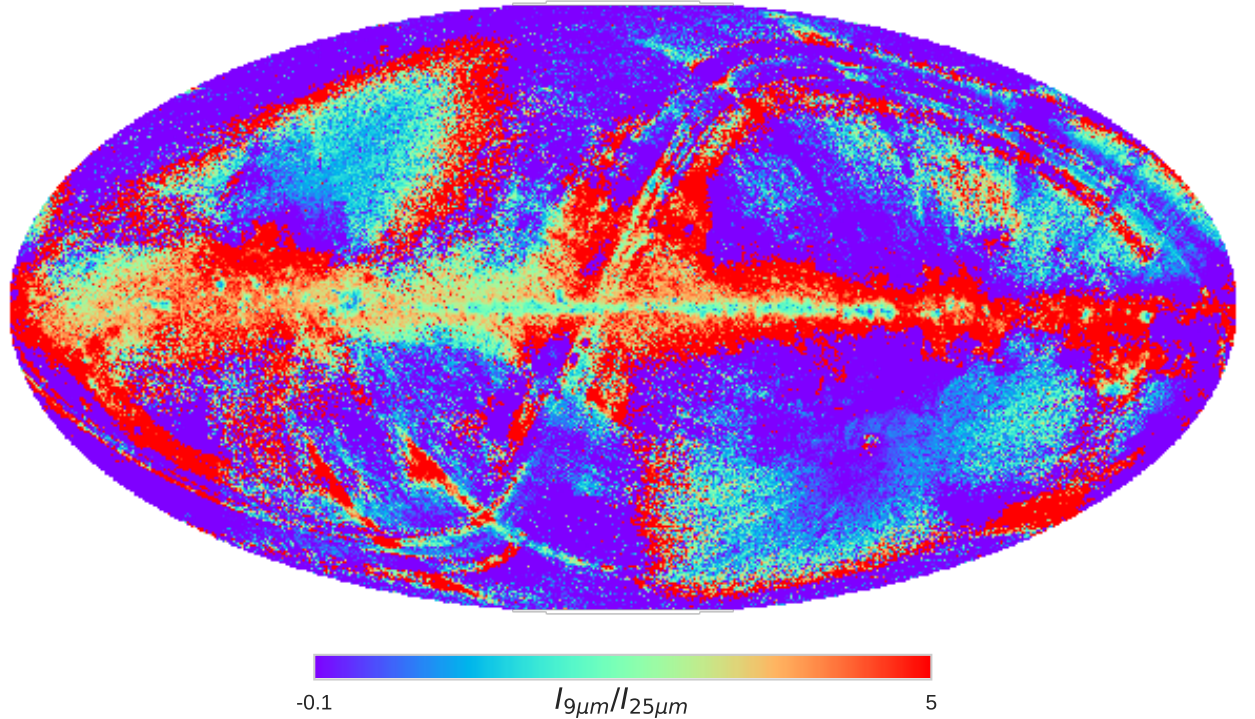


Figure 2.6: AKARI/IRC 9 μm to IRAS 25 μm intensity ratio.

543 2.3 Infrared Astronomical Satellite (IRAS)

544 Data from the IRAS (Neugebauer et al. 1984) all-sky surveys are used to supplement the similarly-
 545 centered AKARI photometric bands. The IRAS 12 μm band is similar to the IRC 9 μm band in terms
 546 of the sky coverage, central wavelength, and especially in that both surveys are heavily dominated by
 547 zodiacal light. We use the Improved Reprocessing of the IRAS Surveys (IRIS) (Miville-Deschénes
 548 & Lagache 2005), which have undergone a zodiacal-light removal. The Zodiacal light model, however
 549 differs between the two bands. The IRAS Zodi-subtraction is primarily based on the Kelsall et al.
 550 (1998) model. Although WISE provides higher resolution than IRAS, we do not utilize the WISE
 551 data because we found the WISE all-sky 12 μm product to essentially trace the Planck HFI 857 GHz
 552 map, at 1 degree angular resolution. Hensley et al. (2016) had noted that this scaling of the WISE
 553 map may artificially suppress actual PAH-related variations at low resolution. Moreover, since we are
 554 conducting our analysis at 1 degree resolution in order to match the AME data, the higher resolution
 555 offered by WISE is not a significant advantage.

556 2.4 Planck COMMANDER Parameter Maps

557 We utilize the COMMANDER-Ruler astrophysical component separation maps (Planck Collaboration et al. 2014c), from the Planck Collaboration’s Public Data Release 2 (hereafter, PR2)(Planck
558 Collaboration et al. 2016a). These contain estimates of known microwave foreground components
559 (free-free, synchrotron, thermal dust emission contributions to the Planck photometric bands. Fig. 2.7
560 demonstrates the correlatedness of these component maps, taken as provided in the PR2 archive.
561 Without considering noise levels or variations of scale, we see evidence these major components are
562 correlated with one another. In the case of free-free emission, von Hausegger & Liu (2015) found that
563 by taking S/N ratios into account, the correlation between COMMANDER free-free and AME com-
564 ponents turns negative. More generally they suggest that the intercorrelations between these products
565 varies with scale. We will first describe the ‘non-AME’ components, so as to not give any indication
566 that their estimation is trivial.

568 2.4.1 Synchrotron

569 While the Planck observations themselves do limit our resolution when assessing the AME - it is
570 the primary constraint on synchrotron emission, 408 MHz map by Haslam et al. (1982) that is the
571 major resolution limiting factor. While an impressive early effort to reveal the low-frequency sky,
572 (Haslam et al. 1982) is limited to an approximately 1 degree resolution. The map also contains many
573 artifacts. For the time being however, it is still the most synchrotron-dominated all-sky map available,
574 and for this reason PC15X included it in their COMMANDER component separation. Enhanced
575 synchrotron mapping efforts are currently in progress by the ‘The final synchrotron product produced
576 by COMMANDER (hereafter, PCSync) highly resembles the Haslam et al. (1982) map, however it
577 is also demonstrated PCSync does not fully capture the synchrotron signal. This can be visualized
578 by inspecting the PCAME:PCdust ratio map (see Fig. 2.12), which Hensley et al. (2016) describe as
579 containing synchrotron emission patterns at high latitudes.

580 2.4.2 Free-free emission

581 Unlike the PCSync component, the fitting of the Planck COMMANDER free-free component map
582 (hereafter, PCff) does not employ any free-free dominated emission map, even though an earlier
583 Planck AME paper (Planck Collaboration et al. 2014d) had employed the H- α map by Reynolds

	AMEvar	AMEfix	AMErad	AMEfreq	ff	Sync	$I_{dust}(545)$	T	B
AMEvar	1	0.81	1	-0.37	0.64	0.68	0.8	-0.52	0.39
AMEfix	0.81	1	0.83	-0.011	0.73	0.71	0.89	-0.59	0.42
AMErad	1	0.83	1	-0.32	0.66	0.7	0.83	-0.54	0.4
AMEfreq	-0.37	-0.011	-0.32	1	0.023	0.063	0.093	-0.051	0.042
ff	0.64	0.73	0.66	0.023	1	0.56	0.74	-0.51	0.44
Sync	0.68	0.71	0.7	0.063	0.56	1	0.74	-0.41	0.38
$I_{dust}(545)$	0.8	0.89	0.83	0.093	0.74	0.74	1	-0.69	0.38
T	-0.52	-0.59	-0.54	-0.051	-0.51	-0.41	-0.69	1	-0.38
B	0.39	0.42	0.4	0.042	0.44	0.38	0.38	-0.38	1

Figure 2.7: r_s cross correlation matrix of the PCCS maps: temperature T , emissivity index β , and amplitude at 545 GHz $I_{dust}(545)$ of thermal dust; intensity of free-free emission ff ; intensity of synchrotron emission at 4 MHz $Sync$; intensity of the AME var. freq. component AME at 22.8 GHz.

584 et al. (1998). Uncertainties in this map arise from uncertainties in the gas temperature, and the Gaunt
585 factor. This emission source is the dominant source of confusion with AME, especially for Hii regions
586 (Planck Collaboration et al. 2014d,c; Paladini et al. 2015).

587 **2.4.3 Thermal dust emission**

588 “Thermal dust emission” in the COMMANDER context refers to dust emission in the Rayleigh Jeans-
589 regime, as the COMMANDER fitting does not include photometric constraints on the thermal emis-
590 sion peak, or consider small grain emission on the Wiens side. This component essentially involves
591 the fitting of a modified blackbody curve (Eq. 1.2.1.) to the Planck Photometry. This approach
592 however results in an apparent anti-correlation between β and T (Fig. 2.7). Whether or not this anti-
593 correltion is genuine is still unsettled in the literature. In any case, we do not utilize the β and T , only
594 the dust intensity at 545 GHz (I_{dust}) parameter map.

595 **2.4.4 AME data**

596 The COMMANDER map release also provides an “AME component map”, which presumes that
597 AME originates from spinning dust. While acknowledging that such a decomposition lacks a strong
598 physical interpretation, Planck Collaboration et al. (2016b) break the AME into two components:
599 a spatially varying peak frequency component, and a spatially constant peak frequency component.
600 As seen in Fig. 2.8, virtually all of the fitted peak frequencies for AME_{var} are beyond the reach of
601 WMAP and Planck. Only the fitted global frequency, 33.5 GHz for the spatially constant component,
602 is covered. However they note that the combined components, per pixel, would have an average peak
603 at least within the WMAP coverage range. In general, AME_{var} is the dominant component, account-
604 ing for approximately 90% of the total AME intensity at a given frequency, indicated by the full-sky
605 histograms in Fig. 2.9. As they are provided in PR2, the intensities are in fact the fitted spinning
606 dust profiles for each pixel, evaluated at reference frequencies: 22.8 GHz for AME_{var} , 41 GHz for
607 AME_{fix} (for convenient comparison to the WMAP total intensity maps at those frequencies). Fig. 2.9
608 in fact indicates our own re-evaluation of the fitted spinning dust SEDs at their peak frequencies, as
609 the reference frequencies to not have any special physical relevance. This conversion does not have
610 a significant effect on the results in the chapters to follow, except in the case of some outlying pixels
611 with very low peak frequencies, easily seen in the map of the fitted frequencies in Fig. 2.10. However
612 on comparison to point source masks by Planck, we find that these outliers correspond to intensity

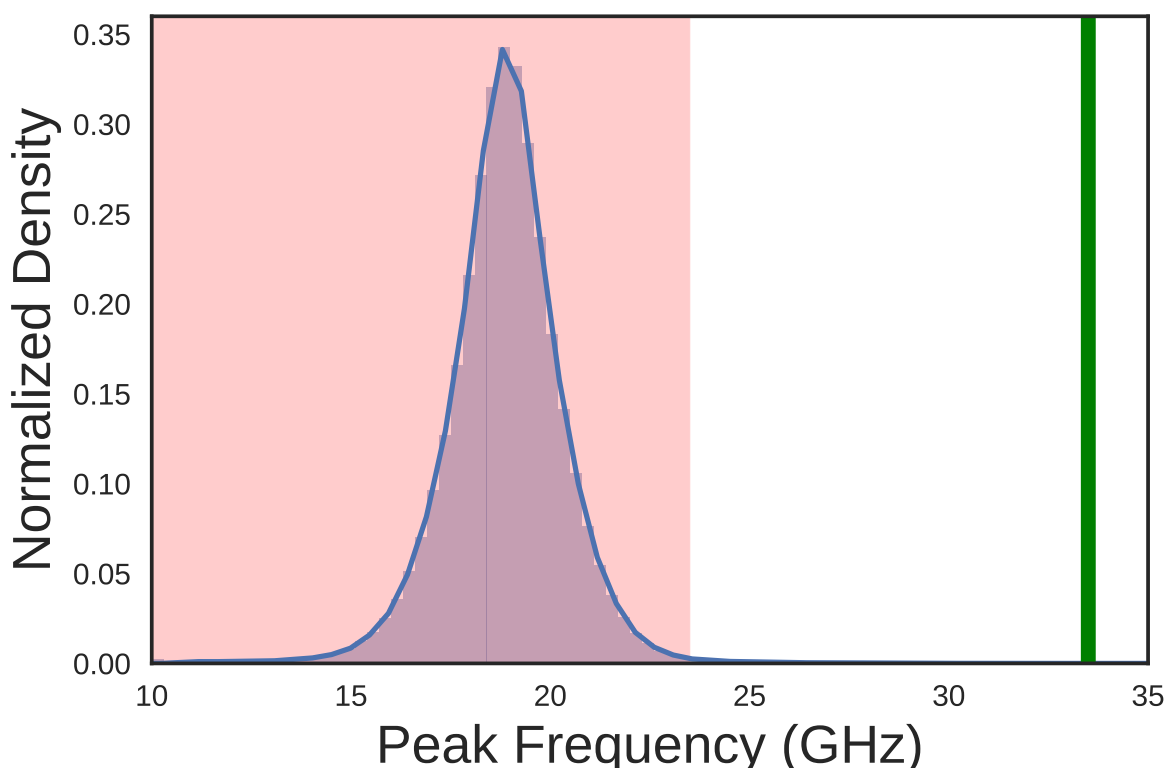


Figure 2.8: The peak frequencies of the varying component AME_{var} . The pink shaded region indicates frequencies not covered by either WMAP or Planck. The green line at 33.5 GHz indicates the peak frequency of AME_{fix} .

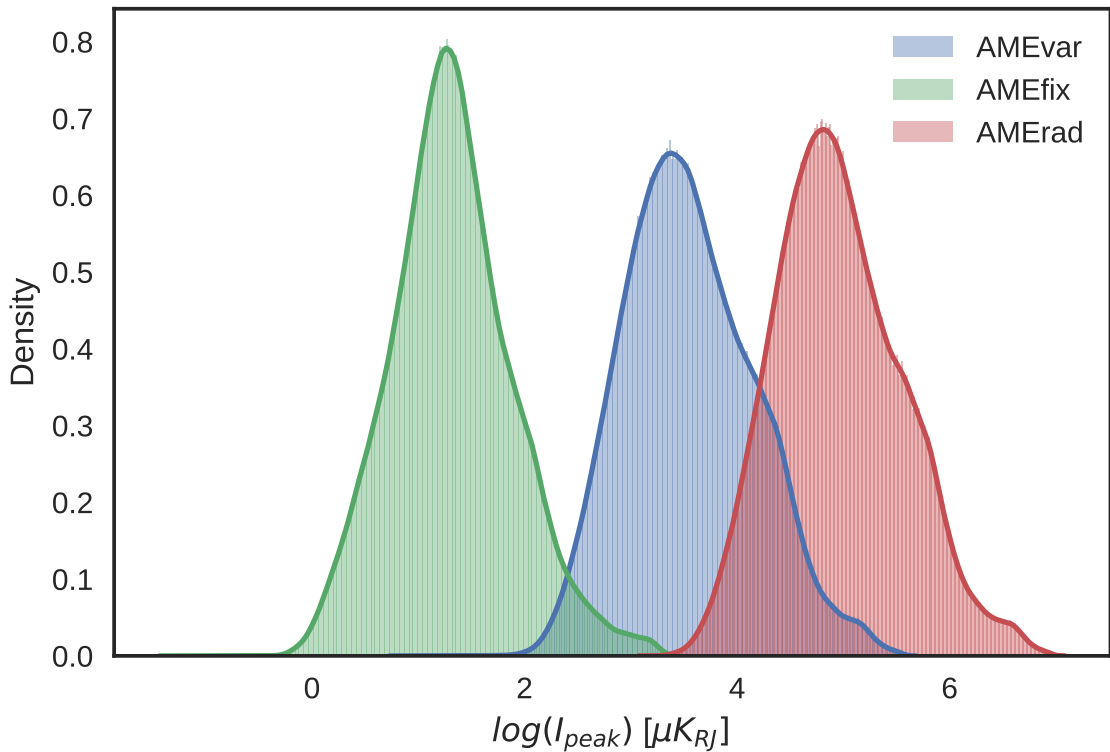


Figure 2.9: Histograms of the peak intensity AME maps calculated from the original COMMANDER-AME reference frequency maps. The dominant component, AME_{var} is indicated in blue, for all pixels in the map, with their spinning dust intensities evaluated their peak frequencies (see Fig. 2.8.) AME_{fix} gives the peak intensity of the spatially-constant frequency component, indicating it is essentially always the weaker component.

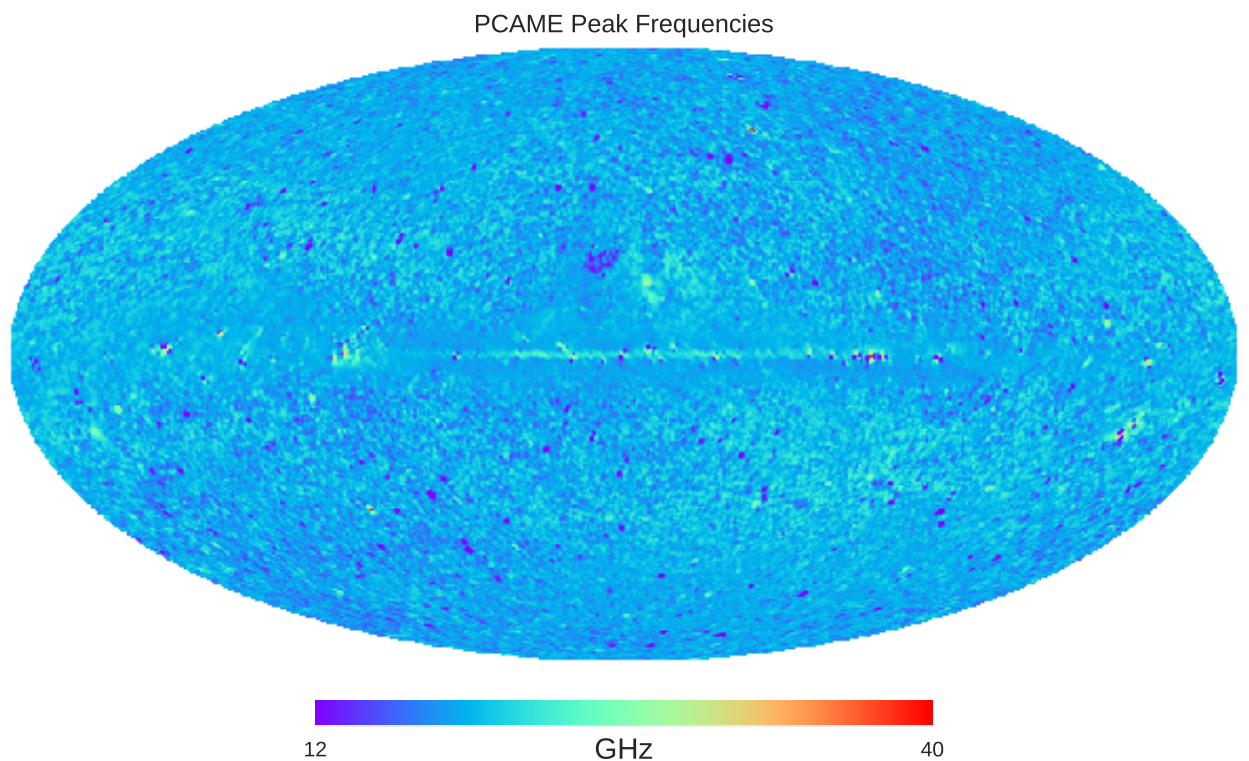


Figure 2.10: All-sky map of the peak frequencies of the varying component AME_{var} , corresponding to Fig. 2.8. Virtually all of the purple regions of the map correspond to pixels flagged for point sources in the LFI data. There are very few notable structures in the frequency map overall, other than the galactic plane itself, ρ Ophiuchus, and Perseus.

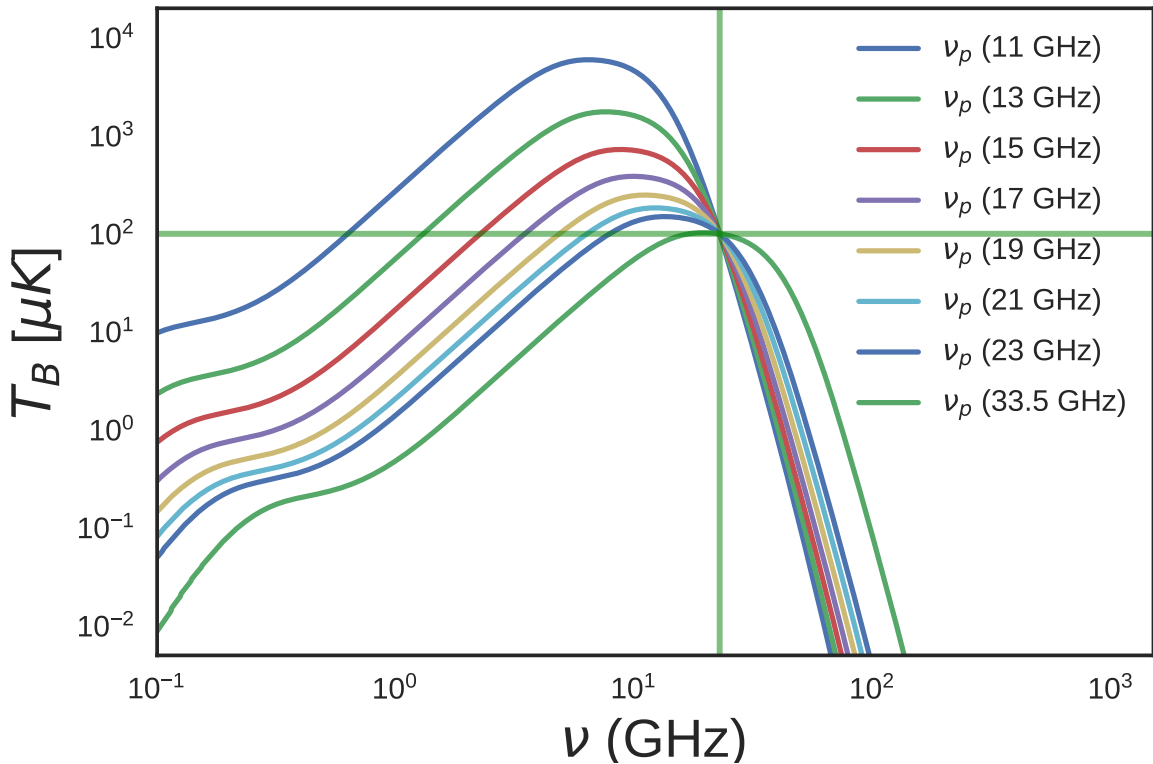


Figure 2.11: Spdust template spinning dust profiles fitted by PC15X when calculating AME_{var} . The reference frequency, 22.8 GHz is indicated by the vertical green line. Each template has the same AME_{var} amplitude of $100 \mu\text{K}$, indicated by the horizontal green line, plotted to highlight the potential deviation between AME_{var} and the actual peak intensity.

613 outliers in the LFI 30 GHz map. This is not readily apparent when viewing the AME_{var} , evaluated at
 614 22.8 GHz, as it is provided in Planck Collaboration et al. (2016b).

615 Spinning dust fitting

616 The actual spinning dust SED which is fitted to the Planck data by is indicated by Fig. 2.11, which
 617 we have reproduced from the original template provided in Ali-Haïmoud et al. (2009). PC15X fit
 618 the AME by applying a frequency shift and intensity shift parameter to this template. The physical
 619 parameters of the 'spdust' model itself are not directly varied in PC15X. In any case, the spinning dust
 620 model SED shape does not show significant variation from environment to environment (Ali-Haïmoud
 621 et al. 2009). Because of the phenomenological approach of the AME fitting method, the PC15X authors
 622 themselves suggest caution in deriving conclusions from comparisons with the COMMANDER AME
 623 map. However it is the most thorough all-sky component separation currently available, and has
 624 not been well analyzed relative to the wavelength range of IR all-sky maps produced. Improving
 625 on the COMMANDER AME map will likely require lower frequency constraints (in the red-shaded

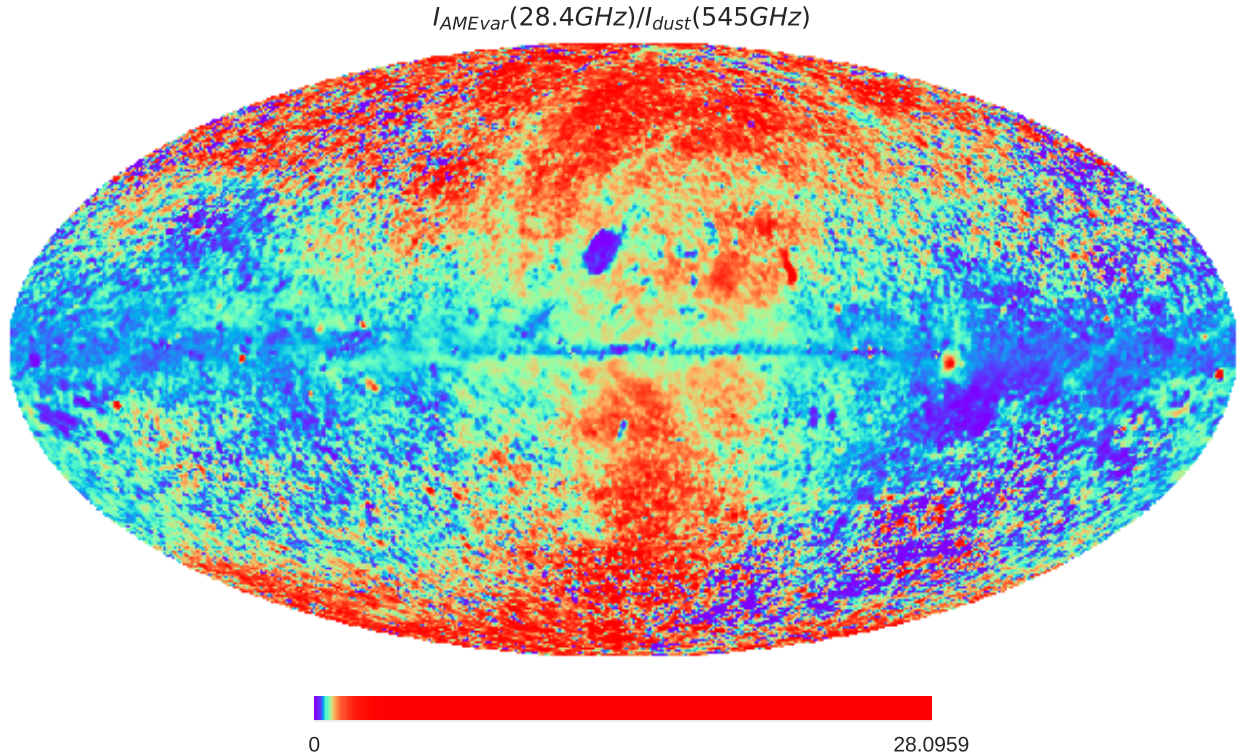


Figure 2.12: All-sky map of the ratio of two COMMANDER components- the frequency-varying AME component divided by the intensity of thermal dust emission at 545 GHz. There are some recognizable AME emission regions, such as λ Orionis. Large-scale patches of AME excess are noted to correspond to synchrotron emission (Hensley et al. 2016)

portion of) and/or higher resolution observations of not only the AME itself but the contribution from synchrotron and free-free emission. This way some of the inherent degeneracies between free-free, synchrotron, thermal dust, and AME parameters may be able to be broken.

2.5 All-sky Data Processing

The HFI, FIS, and IRIS maps used here are downloaded from their respective online repositories, as all-sky HEALPix⁶ maps (Górski et al. 2005). NSIDE 2048 maps. In the case of the IRC maps, we first create HEALPix maps from the 4,857 all-sky survey tiles using the Aladin all-sky data visualization platform (Bonnarel et al. 2000). NSIDE 2048 implies an average pixel spacing of $1.7'$. The maps are then degraded to NSIDE 1024 before carrying out a Gaussian-beam smoothing to a 1° FWHM. Map smoothing itself is done in spherical harmonic space, before the maps are transformed back to position space. These steps are handled by the smoothing function contained in the healpy python package. Following the smoothing process, the maps are degraded once more to NSIDE 256, or $15'$

⁶HEALPix core software is described at <http://healpix.sourceforge.net>. The HEALPiX python package “healpy” used in this work is available at: <https://github.com/healpy/healpy>

638 pixel-width⁷. The value of each of the larger NSIDE 256 pixels, comes from the mean of its parent
639 NSIDE 1024 pixels. The purpose of this processing is to ensure that all of the maps have the same
640 resolution as the PR2 AME map.

⁷HEALPix pixel scale rebinning carried out with healpy.ud_grade

⁶⁴¹ Chapter 3

⁶⁴² Analysis of an interesting AME region: ⁶⁴³ λ Orionis

⁶⁴⁴ 3.1 An interesting AME region

⁶⁴⁵ The λ Orionis molecular ring, also known as the Meissa Ring is a massive stucture surrounding the
⁶⁴⁶ λ Orionis O-type star. The ring contains an HII region, ionized by LOrí itself and its OB associates
⁶⁴⁷ (Murdin & Penston 1977). What had been thought of as a starforming region of missing molecular
⁶⁴⁸ gas. At the time Murdin & Penston (1977) even speculated that this could be evidence of an alternate
⁶⁴⁹ starformation pathway, writing: “Notably we need to know if λ Ori is an example of a different mode
⁶⁵⁰ of star formation or [...] simply a case in which the progenitor molecular cloud was exhausted within
⁶⁵¹ the last one or two million years.”

⁶⁵² Maddalena (1986); Maddalena & Morris (1987). (and references therein) noted a ring of material
⁶⁵³ likely being pushed out by the central, historically well-known λ Orionis Association of B-type stars
⁶⁵⁴ and surrounding HII reigon.

⁶⁵⁵ 3.1.1 Where does the ring come from?

⁶⁵⁶ Cunha & Smith (1996) argued that the ring may have resulted from a supernova explosion, further
⁶⁵⁷ speculating that LOrí may have been a companion of the progenitor. λ Orionis is a known binary
⁶⁵⁸ system, however its current companion is the a B-type star. (Murdin & Penston 1977) . The central
⁶⁵⁹ region is heated by the λ Orionis star itself, and the Orion OB association it belongs to (Ochsendorf
⁶⁶⁰ et al. 2015). The region is known to host several young stellar and protostellar objects (Koenig et al.

661 2015).

662 At approx. 10° wide, we can see the outline of the structure even in the low (1° FWHM) resolution
663 PCAME map. The ring shape itself is thought to originate from a supernova, or perhaps combined
664 effects of the entire star formation history of the λ Orionis Association, including the formation of its
665 surrounding HII region (Aran 2009).

666 3.1.2 A well-studied region

667 Although the λ Orionis region has been a popular target for study since approximately the 1980s. Duerr
668 et al. (1982) wrote of the relative lack of work on the overall region: “Surprisingly, this interesting
669 complex has been little studied”. While this seems surprising given the number of works on the region
670 in the literature now, it is really the advent of all-sky missions that have driven more recent interest.
671 The large angular size is such that all-sky surveys were a natural boon for study of such extended
672 structures. WISE especially was a huge source of insight (Koenig et al. 2015). More recently, Planck
673 Collaboration et al. (2016c) strongly highlighted the region as a strong candidate for further AME
674 investigation.

675 3.2 Investigative approach

676 We have carried out an initial comparison of the AME of this region with its mid to far-IR dust
677 emission. The region is shown in Fig. 3.1 as it appears in 1° -smoothed A9 data. Images at each
678 wavelength used here are included as in appendix to this thesis. The ring structure itself indicates
679 excess microwave emission attributed to AME (white contours) while the central region is dominated
680 by free-free emission (Aran 2009; Koenig et al. 2015). Free-free emission coming from the Hii phase
681 surrounding the λ Orionis association dominates the region’s morphology in LFI images. (Planck
682 Collaboration et al. 2016c). Taking the hint from Planck Collaboration et al. (2016c) that this may
683 be among the more reliably component separated regions, we evaluate if there is any preferential
684 relationship between any parameter of dust emission and the AME. Fig. 3.2 shows the expected dis-
685 tribution of free-free emission in the region, assuming that $H\alpha$ line emission is a tracer of microwave
686 free-free. This indicates that free-free is strong within the central region, where radiation fields are
687 more intense, and AME is minimal. The strongest AME follows the ring-shaped morphology outside
688 the central bubble of free-free emission.

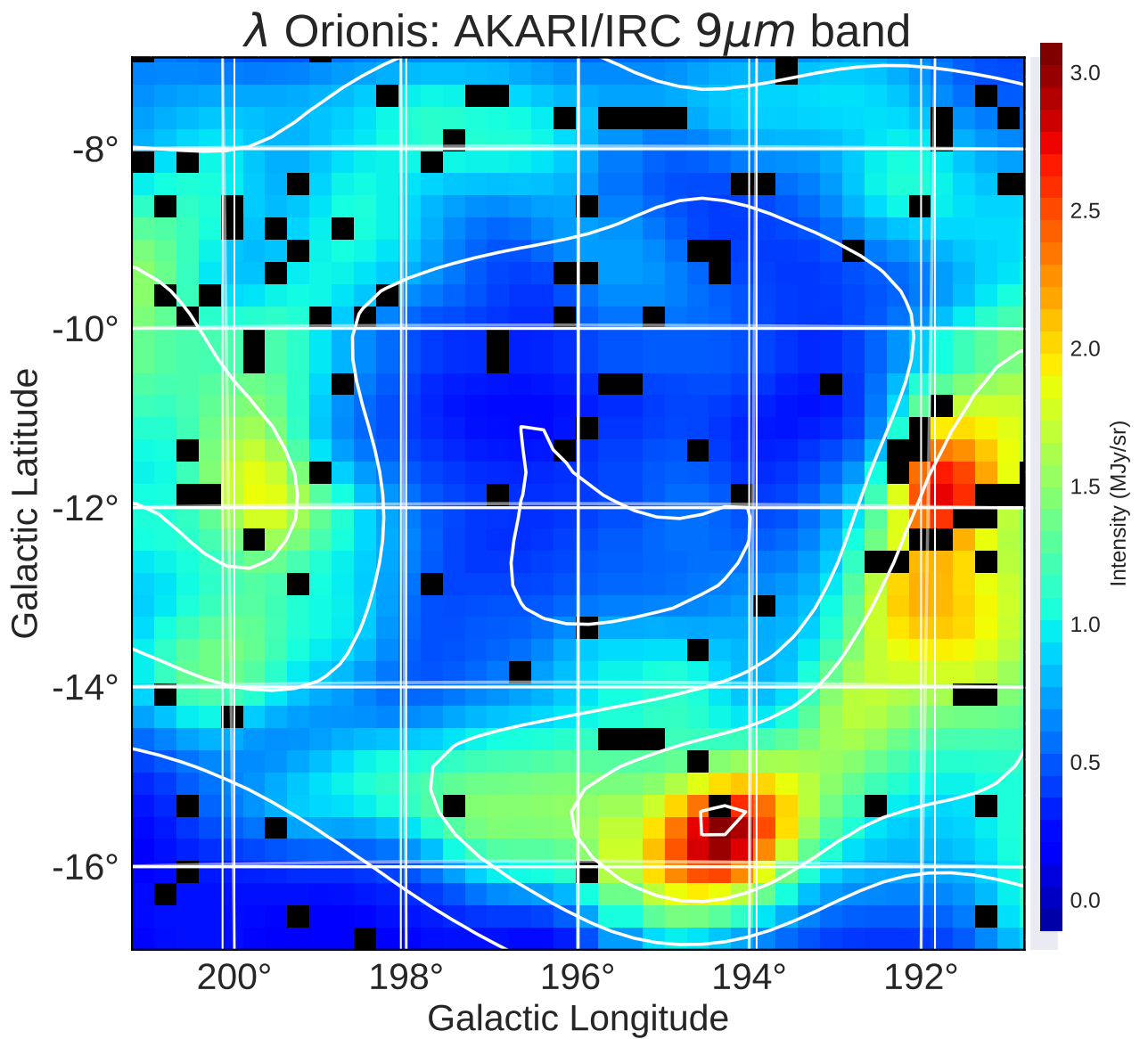


Figure 3.1: λ Orionis as it appears in the AKARI 9 μ m data. Contours indicate the AME, as given by the Planck PR2 AME map. The image is smoothed to a 1° PSF (much larger than the original 10 arcsec map). The λ Orionis star itself is approximately located at the center of the image.

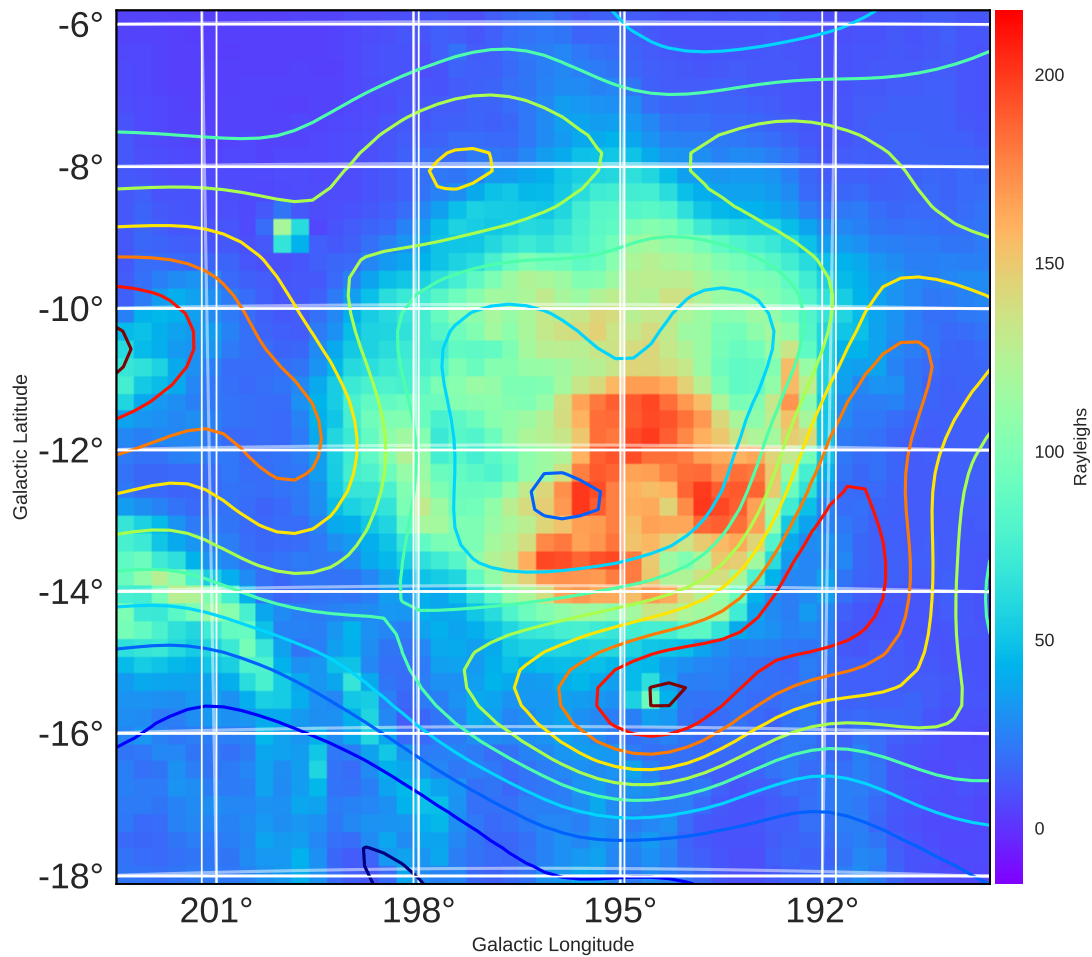


Figure 3.2: λ Orionis as it appears in H-alpha emission by ?. Contours indicate AME emission, from the variable frequency component. The colorbar indicates $H\alpha$ emission in Rayleighs. The field of view is slightly larger than that used for the IR comparison.

689 3.3 Data preparation

690 As indicated in Ch. 2, we use 12 photometric all-sky maps. For the IRC data (A9 and A18), we
 691 produce mosaics of λ Orionis from the individual tiles provided in the internal all-sky archive.¹ For
 692 the other sources, HEALPix all-sky maps are available publicly, at sufficient resolution relative to
 693 their native resolutions.²³⁴

694 3.3.1 Extraction from HEALPix maps

695 For the data obtained via HEALPix maps, we employ the “healpix2wcs” functionality provided in the
 696 “gnomdrizz” python package⁵⁶ A9 and A18 images are produced by regridding the images with the
 697 “montage” software by NASA/IPAC. All of the images for all of the bands are based on a common
 698 FITS header which has a pixel grid spacing equal to the average pixel width in the NSIDE 256
 699 HEALPix scheme. A background estimation and subtraction is made

700 3.3.2 Point-source and artifact masking

701 3.3.3 PSF Smoothing

```
702 import numpy as np
703
704 def incmatrix(genl1, genl2):
705     m = len(genl1)
706     n = len(genl2)
707     M = None #to become the incidence matrix
708     VT = np.zeros((n*m, 1), int) #dummy variable
```

¹IRC all-sky data is still in the proprietary phase at the time of this writing, but should be public by April 2018.

²Planck data was retrieved from the NASA IPAC online archive at http://irsa.ipac.caltech.edu/data/Planck/release_2/all-sky-maps/

³AKARI/FIS data

⁴IRAS/IRIS data

⁵Available at <http://cade.irap.omp.eu/dokuwiki/doku.php?id=software>

⁶“drizzlib” 1.2.2 and earlier were not able to correctly access HEALPix files with multiple fields/columns. See appendix for our recommended workaround.

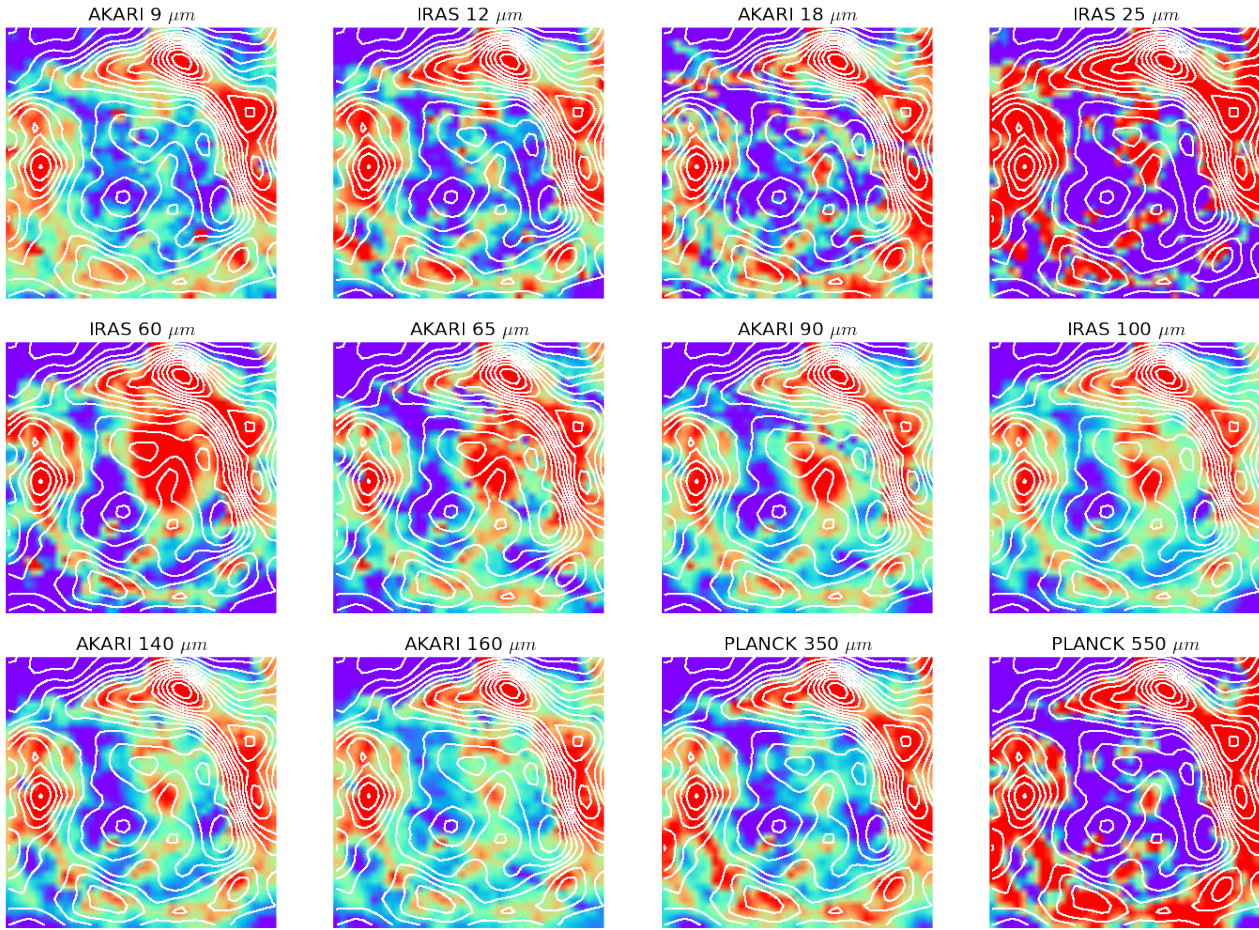


Figure 3.3: A grid of thumbnails showing the λ Orionis region’s structure, at 12 wavelengths, along with AME contours (shown in white contours). Spatial correlation seems to be the best at the shortest and longest wavelengths (AKARI/IRC 9 μm and Planck/HFI 550 μm). The images are smoothed and interpolated for demonstration. Figure 3.1 demonstrates the actual pixel grid used for the SED fitting and intensity correlation tests.

3.3.4 Background subtraction

We estimate an average, flat background level for this region. Although this region is far from the Galactic plane, there is an appreciable background level which must be subtracted. We define two standard background ‘OFF’ zones, indicated in Fig. ??, and use these to determine mean, flat background level. We do not expect the band-by-band correlation tests with the AME to be sensitive to this background subtraction

3.4 Multi-wavelength characterization

Figure 3.3 shows the region in 12 photometric bands, from the mid to far IR, covering key dust emission regimes as described in Ch. 2. Contours indicate the region’s shape in the PCAME map. Figure 3.4 shows IR to AME cross correlation plots, for all pixels within the 10° by 10° λ Orionis

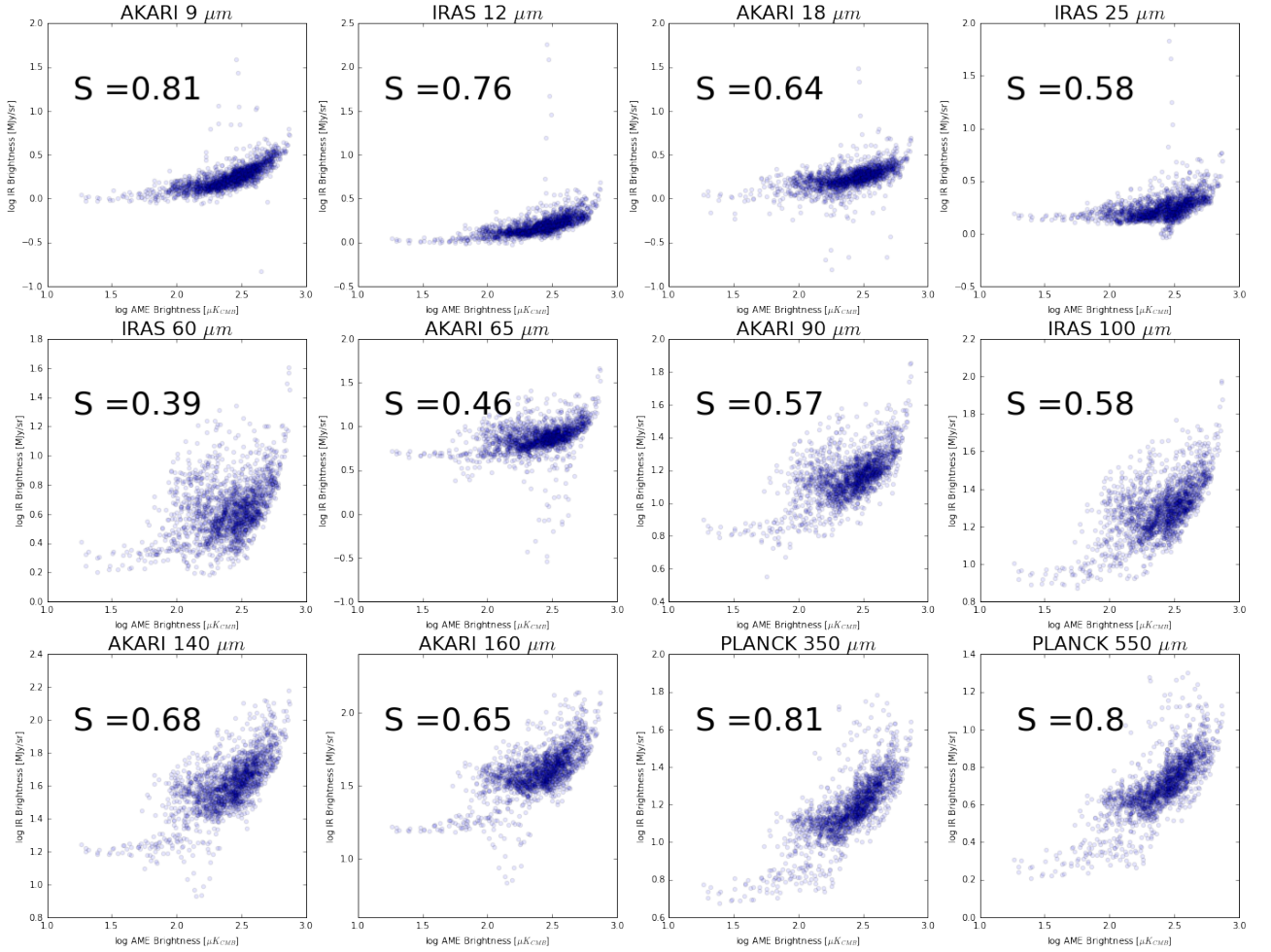


Figure 3.4: Intensity cross-correlation for all pixels in the λ Orionis cut-out region. r_s indicates the Spearman rank correlation coefficient for each plot.

719 region. The correlation matrix results corresponding to data shown in Fig. 3.4, are shown in Fig. 3.5.
 720 The correlation is most clear for the shortest and for the longest wavelength bands, and weakens the
 721 most at around 60 μm . The weakening of the correlation score appears to come from brighter 25 to
 722 90 μm emission within the ring. The spectrum is consistent with warm thermal dust emission, heated
 723 by λ Orionis and its associates. The ring structure itself appears relatively consistent accross all of
 724 the IR bands.

725 3.4.1 Bootstrap analysis

726 To assess the robustness of the correlation scores, we employ the Bootstrap re-sampling approach,
 727 first introduced by Efron (1979). This involves creating random re-sampled sets of the data. We use
 728 the 'with replacement' approach, meaning that a data point may be selected multiple times in a single
 729 re-sampling iteration. The size of the re-sampled set is the same is the input set size. For each random
 730 set we run a correlation test, resulting in a distribution of correlation coefficient. This allows us to

	A9	1	0.93	0.94	0.84	0.75	0.78	0.64	0.66	0.72	0.85	0.84	0.92	0.9	0.89	0.58
D12	0.93	1	0.97	0.83	0.84	0.83	0.76	0.74	0.81	0.91	0.89	0.93	0.91	0.84	0.6	
I12	0.94	0.97	1	0.84	0.82	0.85	0.78	0.77	0.84	0.93	0.92	0.93	0.91	0.85	0.62	
A18	0.84	0.83	0.84	1	0.89	0.91	0.68	0.57	0.67	0.77	0.75	0.72	0.69	0.61	0.39	
D25	0.75	0.84	0.82	0.89	1	0.97	0.77	0.58	0.7	0.77	0.76	0.69	0.66	0.56	0.41	
I25	0.78	0.83	0.85	0.91	0.97	1	0.79	0.62	0.73	0.8	0.79	0.7	0.66	0.58	0.43	
D60	0.64	0.76	0.78	0.68	0.77	0.79	1	0.88	0.94	0.86	0.86	0.67	0.61	0.48	0.57	
A65	0.66	0.74	0.77	0.57	0.58	0.62	0.88	1	0.96	0.9	0.88	0.76	0.7	0.58	0.62	
A90	0.72	0.81	0.84	0.67	0.7	0.73	0.94	0.96	1	0.94	0.93	0.8	0.75	0.63	0.65	
A140	0.85	0.91	0.93	0.77	0.77	0.8	0.86	0.9	0.94	1	0.99	0.91	0.86	0.75	0.63	
A160	0.84	0.89	0.92	0.75	0.76	0.79	0.86	0.88	0.93	0.99	1	0.89	0.85	0.73	0.63	
P857	0.92	0.93	0.93	0.72	0.69	0.7	0.67	0.76	0.8	0.91	0.89	1	0.99	0.89	0.62	
P545	0.9	0.91	0.91	0.69	0.66	0.66	0.61	0.7	0.75	0.86	0.85	0.99	1	0.89	0.59	
AMEvar	0.89	0.84	0.85	0.61	0.56	0.58	0.48	0.58	0.63	0.75	0.73	0.89	0.89	1	0.63	
AMEfix	0.58	0.6	0.62	0.39	0.41	0.43	0.57	0.62	0.65	0.63	0.63	0.62	0.59	0.63	1	
	A9	D12	I12	A18	D25	I25	D60	A65	A90	A140	A160	P857	P545	AMEvar	AMEfix	

Figure 3.5: r_s correlation matrix for all of the data used in the λ Orionis analysis.

estimate error bars for the correlation scores. We carry out bootstrap correlation tests for each IR band's intensity vs. the AME intensity. The data are resampled 10,000 times for each correlation test. This is repeated for both r_s and r_p based tests. The distributions of the bootstrap resamplings are shown in Fig. 3.6. For both test cases, the best correlations are the longest and shortest wavelength bands. In the r_p case, the strongest correlation is the A9 band vs the AME.

3.5 Comparison with SED Fitting

We performed a full dust SED fitting on the λ Orionis photometry, according to the dust model by Galliano et al. (2011) (to be thoroughly introduced in Galliano, et al., in prep.) We used a mixture of silicate and carbonaceous dust, silicate dust, the two dominant categories of interstellar dust as described in Ch. 1. However, instead of the graphite-based carbon dust invoked by the canonical Draine & Li (2007b) model (DL07), we assume amorphous carbon. This choice is an attempt to account for the “sub-mm excess” of dust emission, reported by Israel et al. (2010); Bot et al. (2010), in the Large Magellanic Cloud (LMC). The increased emissivity of amorphous carbon (a factor of 2-3 more than DL07) allows a better fit to Herschel observations of the LMC (Galliano et al. 2011), and Planck observations of the Milky Way (Planck Collaboration et al. 2016d). We assume that the radiation field heating this dust mixture is the Galactic ISRF (Mathis et al. 1983), scaled by a factor U . We also assume, following Dale et al. (2001), that the dust is exposed to a distribution of starlight intensity, distributed as:

$$dM_{dust} \propto U^{-\alpha} dU \quad (3.5.1)$$

between U_{min} and U_{max} , where U_{min} , U_{max} and α are free parameters. We utilize both the Bayesian dust SED fitting approach by Galliano (in prep.), and a least-squares analysis. The SED fitting accounts for estimates of the respective calibration uncertainties, and the spectral response curves (Fig. 2.1). As outputs, metrics of the total dust mass M_{dust} , PAH mass M_{PAH} , ionized PAH mass M_{PAH+} , and ISRF intensity U are produced. We only carry out the fitting for unmasked pixels. We are primarily interested in which of the correlations M_{dust} vs. I_{AME} or M_{PAH} vs. I_{AME} is stronger. Two sample fitting results are shown in Figs. 3.7, and 3.8. Performing such fits for all of the pixels, we are able to see how I_{AME} varies with the bulk dust physical characteristics of the region. Fig. 3.9 shows the fitted dust mass per pixel, relative to the AME intensity. AME intensity is scaled by the ISRF intensity U . Although spinning dust emission is not predicted to vary directly with U , we con-

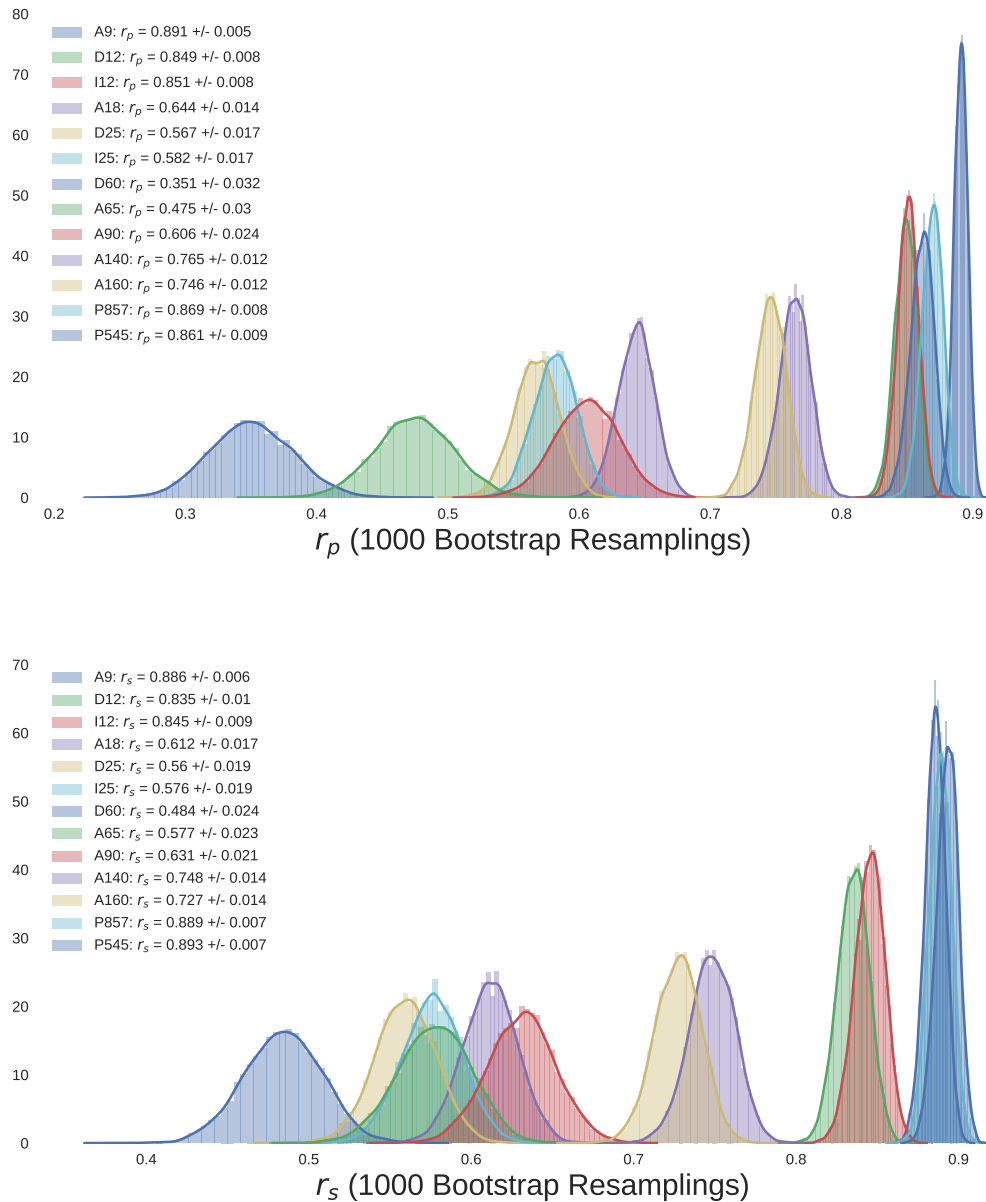


Figure 3.6: Re-sampled (Bootstrap) correlation tests for IR emission in λ Orionis vs. AME, for both Spearman and Pearson correlation tests.)

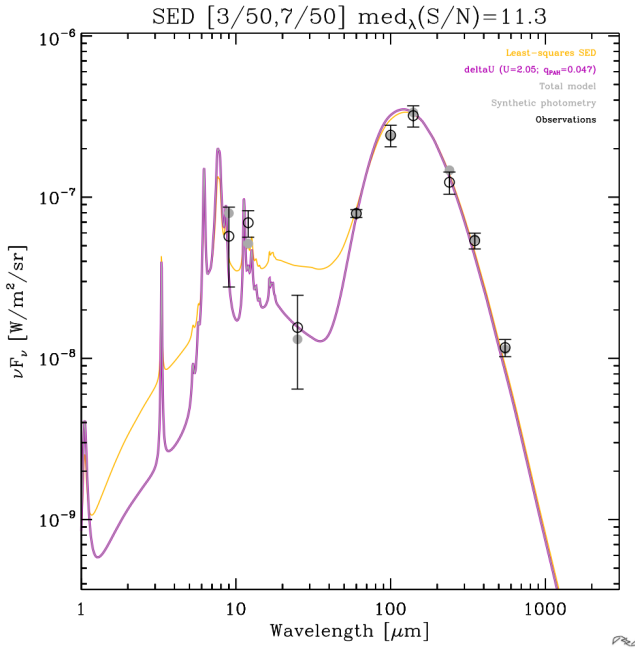


Figure 3.7: Observed (black circles and errors) and synthetic photometry (gray dots) SED of a pixel within λ Orionis, along with the dust SED model fit results. Two SED fits are shown: one for the Bayesian fitting (magenta), and another showing the standard least-squares result for comparison (yellow). The fitted ISRF strength U , and fraction of mass in PAHs, q_{PAH} are also given.

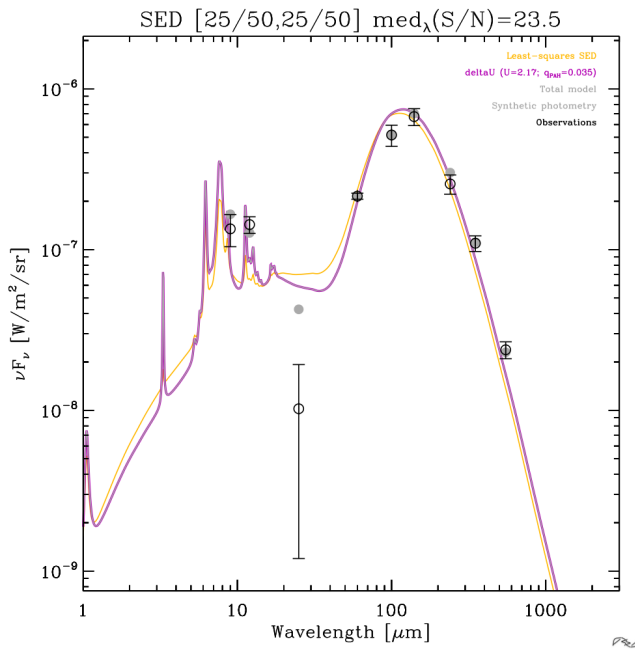


Figure 3.8: The same as Fig. 3.7, but for a different pixel position. Corresponds to galactic coordinates...

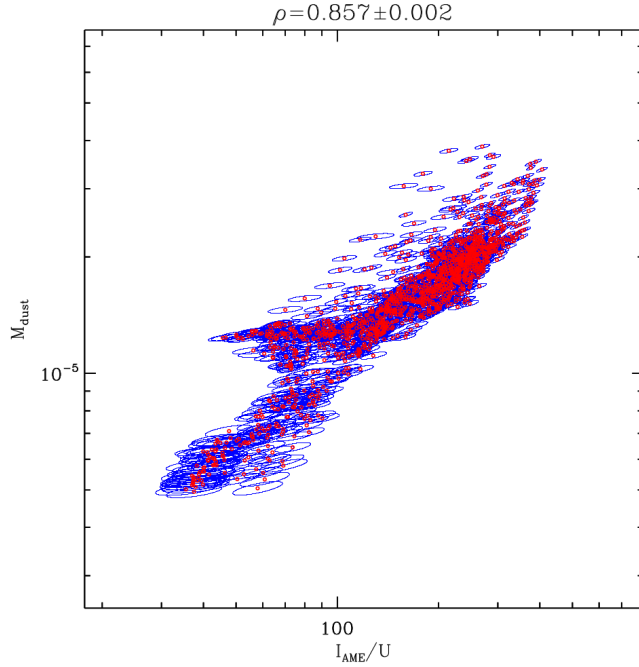


Figure 3.9: Scatter plot with error ellipses generated through the Bayesian SED fitting, of total dust mass M_{dust} vs. I_{AME} scaled by U .

759 sider that the ISRF may serve as a diagnostic of environmental conditions in the ISM. In any case,
760 we find that performing such a scaling improves the correlations with dust mass. Figs. 3.10 and 3.11
761 describe the variation with M_{PAH} and M_{PAH+} . Based on the dust properties derived from these SED
762 fits, we attempt investigate whether any fitted parameter shows a preferential relation with the AME.

763 3.6 Discussion

764 In λ Orionis we found that accross the whole region, A9 emission and P545 emission were the most
765 strongly correlated with AME. This is apparent both in the photometric band analysis, and in the dust
766 SED fitting. The fact that the correlation strengths of PAH-tracing mission and sub-mm emission
767 are similar is in-line with what we have seen in Ysard et al. (2010) and Hensley et al. (2016). In
768 those works, the two relationships (MIR vs. AME and FIR vs. AME) are very close, although
769 these two papers are odds as to which relationship is stronger, and thus in their final interpretation.
770 With the present data and analysis of λ Orionis, we fail to rule out PAHs as carriers of the AME.
771 Fig. 3.12 indicates that although total dust mass and PAH mass are both correlated with AME, there
772 is a strong ($\tilde{100}\%$) probability that PAH mass is the stronger predictor of AME intensity. The results
773 are consistent with a scenario in which PAH mass, cold dust, and the AME are all tightly correlated.
774 Weaker correlation from 25 to 70 μm may indicate that AME is weaker in regions of warmer dust
775 and stronger radiation fields. Such an anti-correlation with harsher radiation are consistent with the

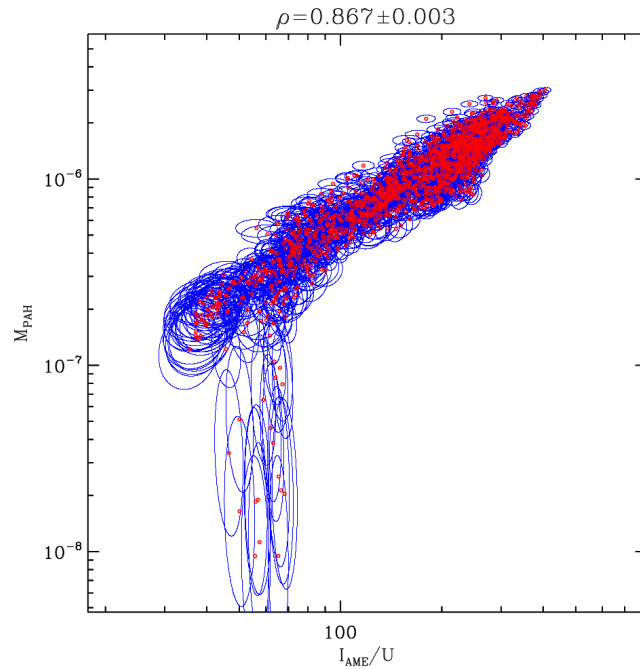


Figure 3.10: The same comparison is given by 3.9, but showing total mass of PAHs (M_{PAH}) rather than total dust mass on the y-axis.

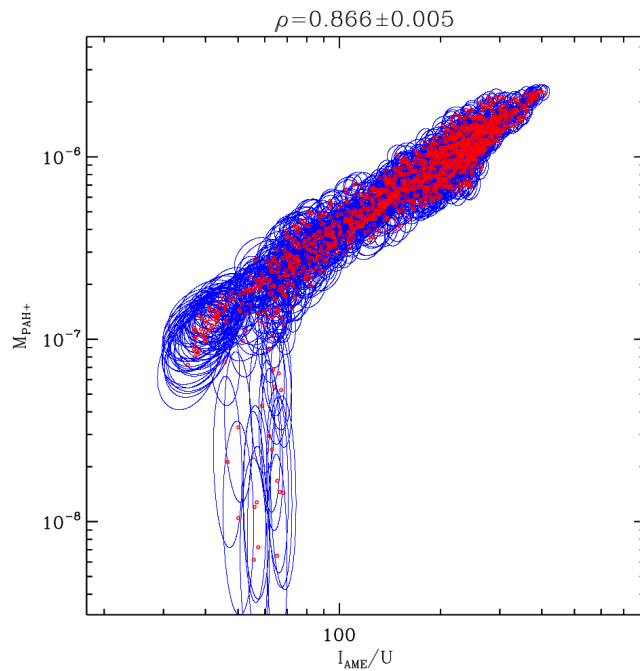


Figure 3.11: The same as in Figs. 3.9 and 3.10 , but specifically comparing an estimate of the ionized component of PAH mass.

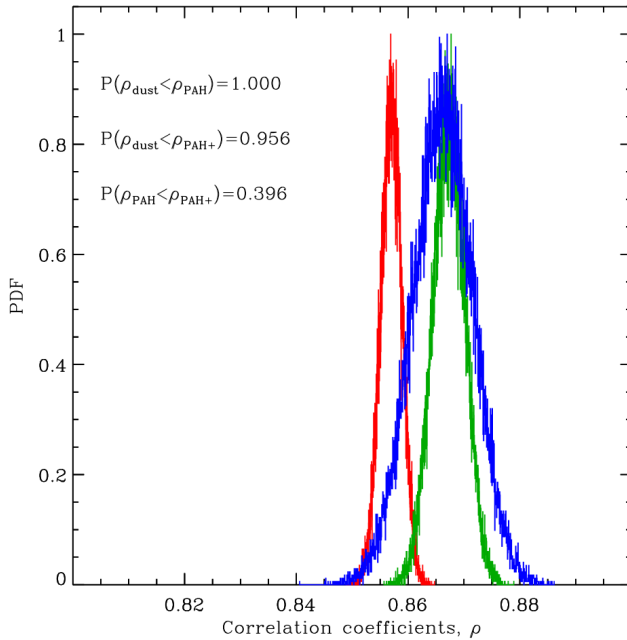


Figure 3.12: The Bayesian correlation probability distributions of Pearson's correlation coefficient (ρ) for the three physical parameters vs. the AME intensity: total dust mass, ρ_{dust} (red); total PAH mass ρ_{PAH} (green); and only the ionized PAH mass ρ_{PAH+} (blue). Also given are the probabilities of either PAH component being better correlated with AME than dust mass, as well as the probability that ionized PAH mass correlates better than total PAH.

776 carriers of AME being destroyed in the central region of λ Orionis, thus leading to substantially
777 decreased spinning dust emission.

778 **3.6.1 PAH Ionization fraction**

779 As described in Ch.2 it is expected that relative variations between the A9 and I12 intensities could be
780 explained by the fraction of PAHs that are charged. Simply examining λ Orionis in intensity, we find
781 that the A9 intensity correlates more strongly with AME than I12 or D12. In the Pearson correlation
782 case, A9 correlates more strongly with AME than any other band. This is consistent with the spinning
783 PAH hypothesis, and taken alone may that the $6.2 \mu\text{m}$ feature emission from ionized PAHs, may be a
784 better predictor of AME intensity.

785 As shown by the dust SED fitting however, the probability distributions (Fig. 3.12) of $r_p(M_{PAH+} : I_{AME})$ does not indicate that ionized PAH mass correlates better with the total PAH mass. Attempts to
786 estimate the PAH fraction based on the available data appear to only add noise relative to $r_p(M_{PAH} : I_{AME})$. The means of the two distributions $r_p(M_{PAH+} : I_{AME})$ and $r_p(M_{PAH} : I_{AME})$ are similar
787 and $r_p(M_{PAH+} : I_{AME})$ shows a wider distribution.

790 Thus the question of whether or not AME comes predominantly from charged PAHs remains

791 open. The fact that A9 correlates more strongly than the 12 μm bands, at least suggests that this topic
792 is worth further investigation. Future wide-area spectral mapping of the λ Orionis region would be
793 able to indicate precisely which PAH features are dominating the A9 and I12 emission, and infer the
794 charged PAH fraction with higher confidence than we can do with wide photometric band ratios. Such
795 observations could be coupled with higher resolution constraints of the AME variation, and a more
796 reliable fitting of the peak frequency of the AME.

797 **Chapter 4**

798 **All-sky Analysis**

799 What we present here is a test of the generalizability of results from Ch.3, which focused on a par-
800 ticular structure on the sky, λ Orionis. We first would like to note that “all-sky analysis” can be a bit
801 misleading. The term tends to lead readers to the idea of a definitive study, answering a particular
802 question for any given position on the sky. While a truly all-sky analysis would be ideal, signal-
803 to-noise constraints (mainly at high galactic latitudes), as well as confusion along the line of sight
804 (mainly in the galactic plane), make a uniformly powerful study of the whole sky very challenging.
805 Here we will indeed show results for the entire sky as a benchmark analysis, but for the core analysis
806 we must mask certain regions dominated by systematic effects in order minimize biases for particular
807 wavelengths.

808 **4.1 Resolution matching**

809 **Smoothing**

810 As in Ch. 3, this approach applies to a spatial resolution of approximately 1° . The resolution limim-
811 tation is imposed by the PC microwave component maps, which list an ‘effective resolution’ of $60'$
812 (Planck Collaboration et al. 2016b). Thus we must apply a smoothing to most of our input datasets,
813 which have native resolutions of a much finer scale (see Tab. 2.1), and Fig. 1.2. The data also come
814 in a wide range of beam shapes with their own degrees of uncertainty, thus we conservatively smooth
815 all of the data in the same way, using a circular Gaussian beam, to have 1° FWHM resolution. we ar
816 We start with an all-sky AME to IR comparison, looking for global patterns among all pixels.

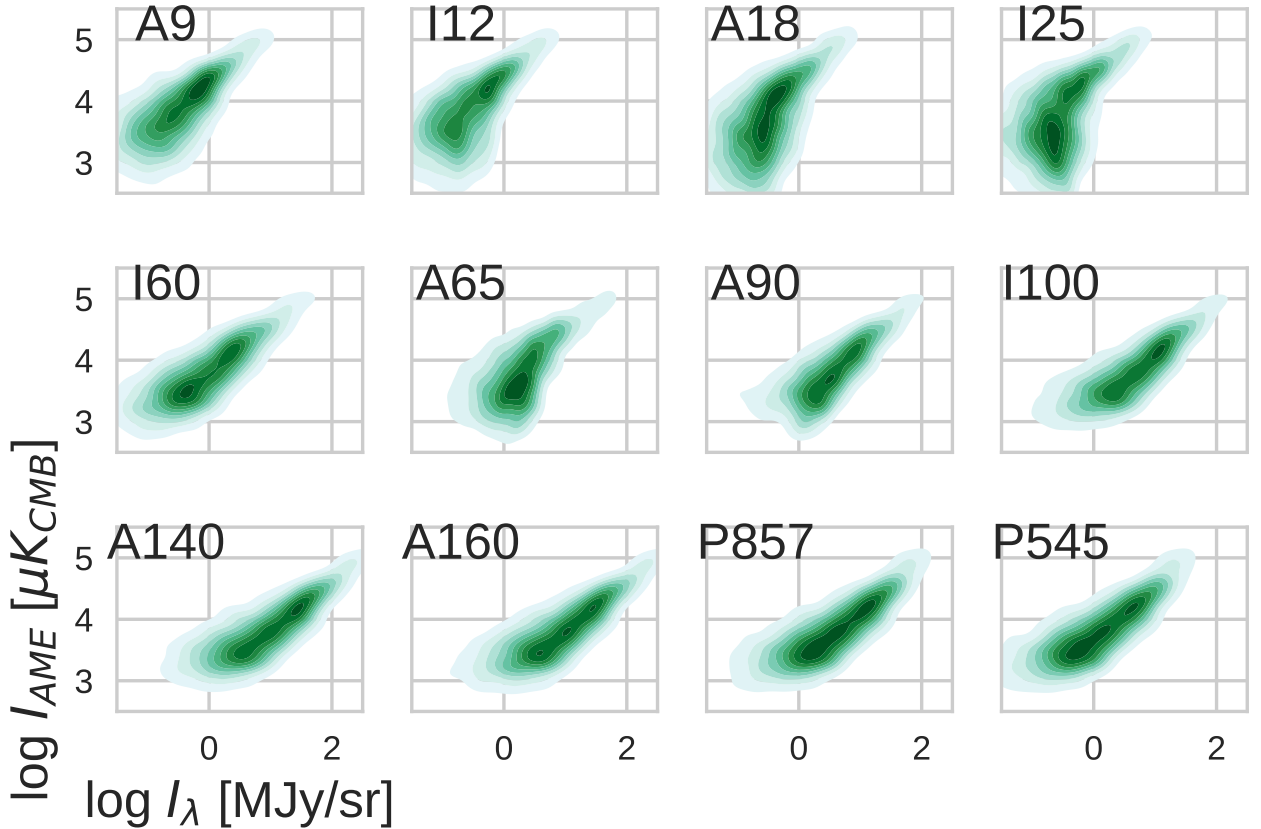


Figure 4.1: Point-density distributions of the AME intensity (Y-axis) vs. the IR bands' intensities. Darker regions indicated higher pixel densities. Only a simple mask of pixels near the ecliptic plane has been applied.

4.2 All-sky cross correlations

In order to look more closely how the the AME to IR relationship varies with wavelength, we first do a comparison without applying any pixel mask, as a benchmark. Fig. 4.1 shows the pixel-density plots of AME vs. the IR bands' intensities. Darker regions show higher pixel densities, unshaded or more lightly shaded regions show low or zero pixel densities. We see immediately that each band shows evidence of a positive trend with AME intensity, as in Ch. 3. For the MIR bands, at lower IR intensities we see the effects of detector noise become dominant, turning into a more defined positive trend with increasing IR intensity. This effect is less pronounced in the FIR. We consider that the IR maps used must not only be compared to the AME, but to each other, to assess multi-wavelength patterns. We also compare the AME and IR maps to ancillary maps, as described in Ch. 2 and Tab. ??.

Fig. 4.2 confirms the weaker trend in the MIR vs. AME, via a cross-correlation matrix, similar to that used in Ch. 3 and Fig. 3.5. This is reflected in the comparison between high and low latitude plots: for pixels $|\beta| > 15\text{deg}$, we see a dramatic effect. In the most extreme case r_s of A18 to AMEvar drops from 0.72 at high latitude, to 0.02 at lower latitudes. $r_s(A9 : \text{AME}_{var})$ drops from 0.79 to

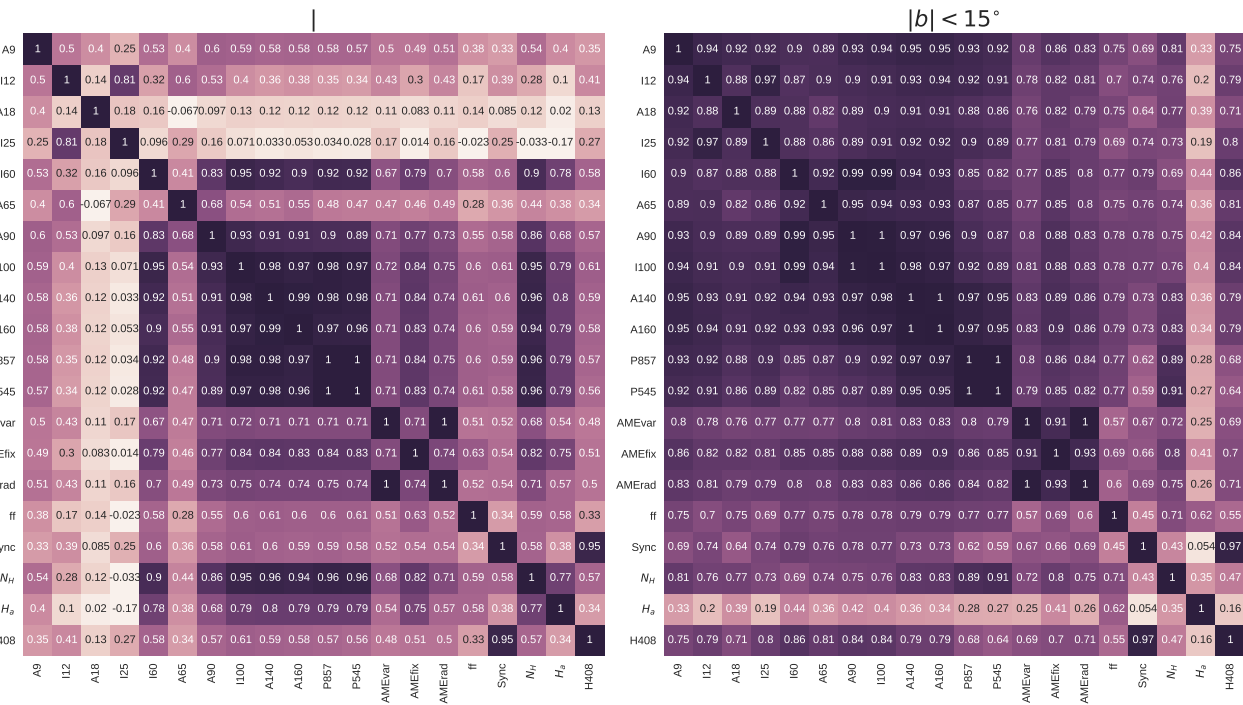


Figure 4.2: ALL-SKY cross-correlation matrix for the 12 infrared bands sampled, as well as the PC component maps described in Ch. 2: the two AME components evaluated at their peak frequencies AME_{var} , AME_{fix} ; Syncrotron, and free-free), and ancillary maps of N_H , H_α emission, and 408 MHz emission Haslam et al. (1982). The color-scale indicates (r_s). Results are based on the unmasked sky, but are split by Galactic latitude: pixels with $|\beta| < 15deg$ (left) and $|\beta| > 15deg$. The color and annotations indicate r_s as in Fig. 3.5.

831 0.42. Correlations between the MIR bands and FIR bands also weaken. Only the the interrelations
 832 between the FIR bands from I60 to P545 remain eseentially latitude independent (with the exception
 833 of A65, which has an especially high noise level.)

834 In the lower latitudes, with $|\beta| < 15deg$, bright emission in and around the galactic plane seems to
 835 homogenize the bands. We see little change from band to band both in terms of the relationship with
 836 AME or with other IR bands. Thus the increase of S/N with decreasing brightness at higher latitudes
 837 has a strong effect on such intensity correlation tests. Bands tracing bright thermal dust emission at
 838 higher latitudes are more robust against this effect. The only case where the trend is reversed, is with
 839 the maps of $N(H)$ and H_α . Both of these maps show higher r_s when compared to high latitude FIR
 840 emission. The next section descibes a pixel-masking strategy designed to mitigate both r_s suppressing
 841 effects from band-to-band S/N variations, and r_s enhancing effects from confusion near the galactic
 842 plane.

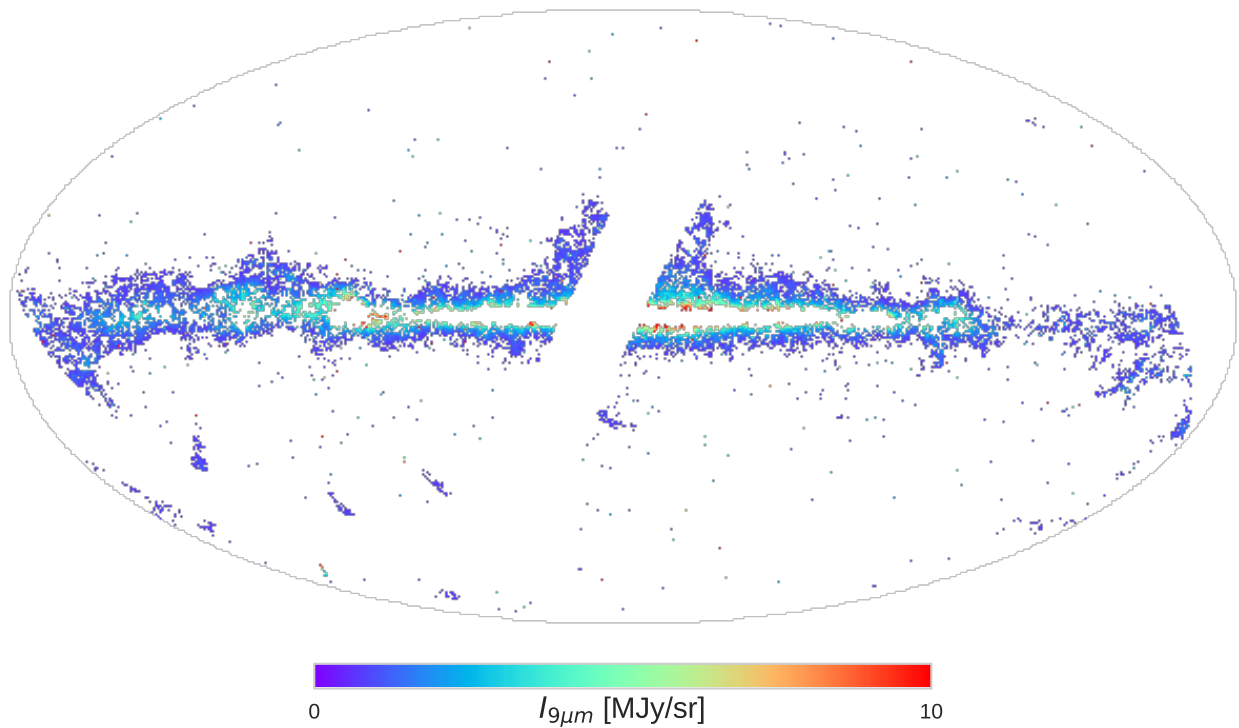


Figure 4.3: All-sky map in A9 emission after applying the combined masks: ecliptic plane, galactic plane, point sources, and pixels with $S/N < 1$. This mask essentially outlines the galaxy, except for the most confused regions.

843 4.3 Masked Comparison

844 For the reasons described in the previous section, we consider that an exhaustive comparsion of the
 845 AME with IR requires the use of a pixel mask. In this section we describe the various masks applied
 846 to the full dataset. We then repeat both the comparisons above (as in Figs. 4.1 and 4.2) for the masked
 847 dataset, and present additional analyses. The full mask, applied to the A9 map, is shown in Fig. 4.3.
 848 The same mask is applied to all maps, including the AME.

849 4.3.1 Pixel mask

850 We prepare a global pixel mask (pixel positions masked in any map are excluded from the analysis).

851 **Zodical light** To keep our analysis comparable to previous works, we exclude pixels within 10° of
 852 the ecliptic plane (Hensley et al. 2016). Even though we use the Zodi-subtracted maps (Kelsall et al.
 853 1998; Kondo et al. 2016; Ootsubo et al. 2016), the Zodi residuals are still problematic (especially in
 854 the MIR.) This corresponds to regions with the heaviest contamination from Zodiacal light, where
 855 Zodi residuals are apparent even with visual inspection for all of the MIR bands used in this study. In

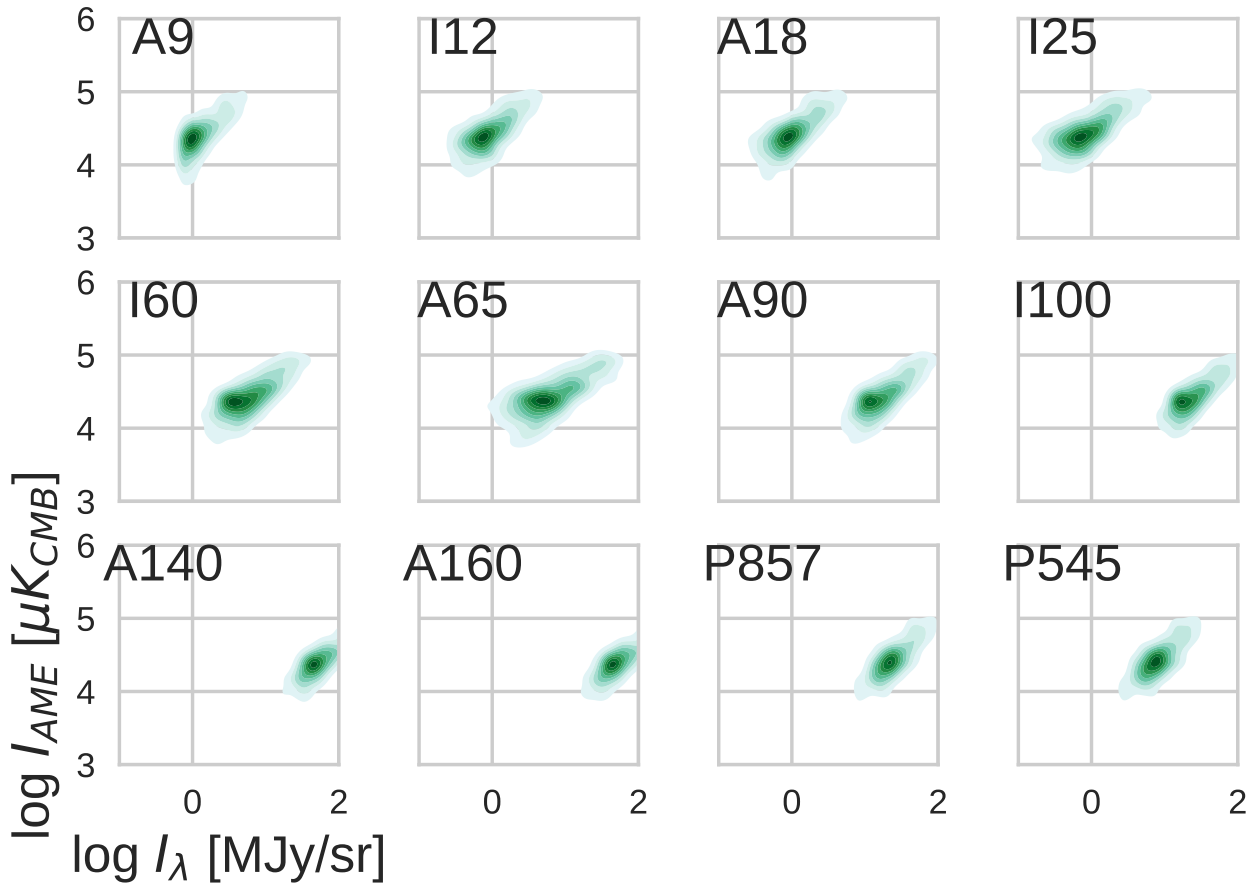


Figure 4.4: The same comparison as shown for Fig. 4.1, but with the mask applied as in Fig. 4.3.

856 Ch. ??, Figs. 2.5, and 2.5 clearly display these residual patterns.

857 **Signal to noise** Some of the bands used lack sufficient sensitivity to trace fainter emission, espe-
 858 cially at higher galactic latitudes. This is mainly an issue for the mid-infrared bands. As such, we
 859 enforce a 3σ threshold for all of the maps— adding to the mask any pixel that has lower than σ
 860 detection in any of the maps. This removes nearly all pixels beyond approx. 15 degrees from the
 861 galactic plane, with the pronounced exception of regions affected by stray moonlight. The extent of
 862 this particular mask is primarily defined by the IRC A9 and A18 maps, which have the highest noise
 863 levels.

864 **Point Sources** The Planck Collaboration provides masks of the pixels they find to include point
 865 sources. We mask pixels which are flagged as being point-source contaminated, in the most heavily
 866 affected maps: Planck/HFI 857 GHz and Planck/LFI 30 GHz. Fig. 4.4 shows point-density plots for
 867 AME_{var} vs. each of the IR bands, after applying the mask described above. As expected with such a
 868 drastic reduction of the number of noise-dominated points, the scatter, especially for the MIR bands,

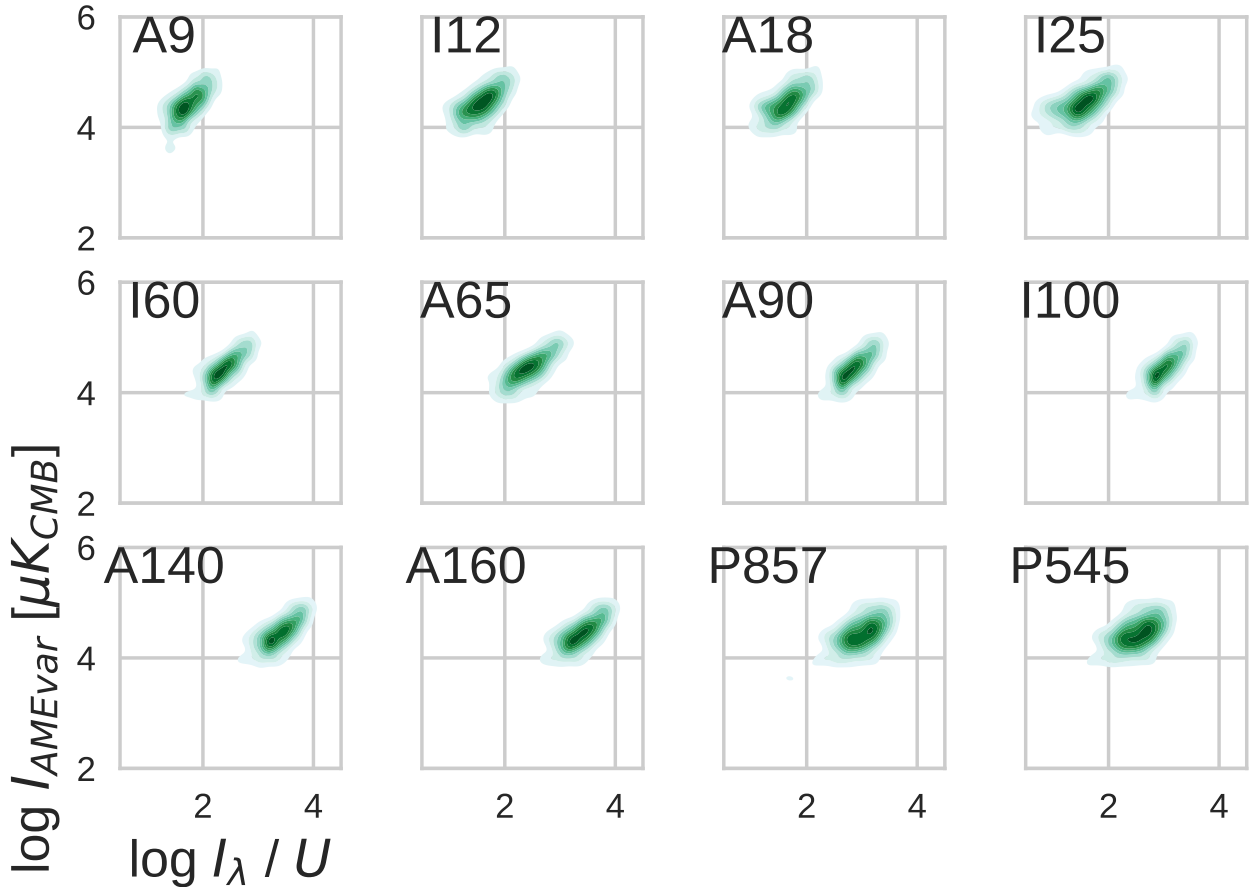


Figure 4.5: Similar comparison to Fig. 4.1, with the IR intensities scaled by U for each pixel.

is reduced. Otherwise the application of the mask does not bring about any special distinction among the bands when compared to the AME. What is notable however is that the persistent weakening of trend of I25 vs. AME, relative to A9 and the FIR bands. Following the logic that the PAH-tracing bands intensity is essentially a product of the ISRF (U) and the column density of PAHs (σ_{PAH}), we redraw the comparison after scaling the IR bands by U . We do this not only for the MIR bands, simply for comparison. We do not have a theoretical prediction as to the relationship between AME intensity and the FIR bands' intensities scaled by U . The pixel density plots for such a comparison are given by Fig. 4.5, which is the same as Fig. 4.4 except for division of the X-axes by U . Corresponding to the plots vs. AME given in Figs. Fig. 4.5 and 4.4, we again perform a cross-correlation matrix test, to understand how the bands relate to one another- not only to the AME. This cross-correlation is done for both intensity, shown by Fig. 4.6 and U normalized intensities shown in Fig. 4.7.

Bootstrap test In addition, for the masked comparison, we carry out a bootstrap analysis similar to that discussed in Ch. 3 and Fig. 3.6. The Spearman rank correlation coefficients r_S of all of the bands, in intensity, vs. the $AMEvar$ component are shown. This is done only for the masked case, due to

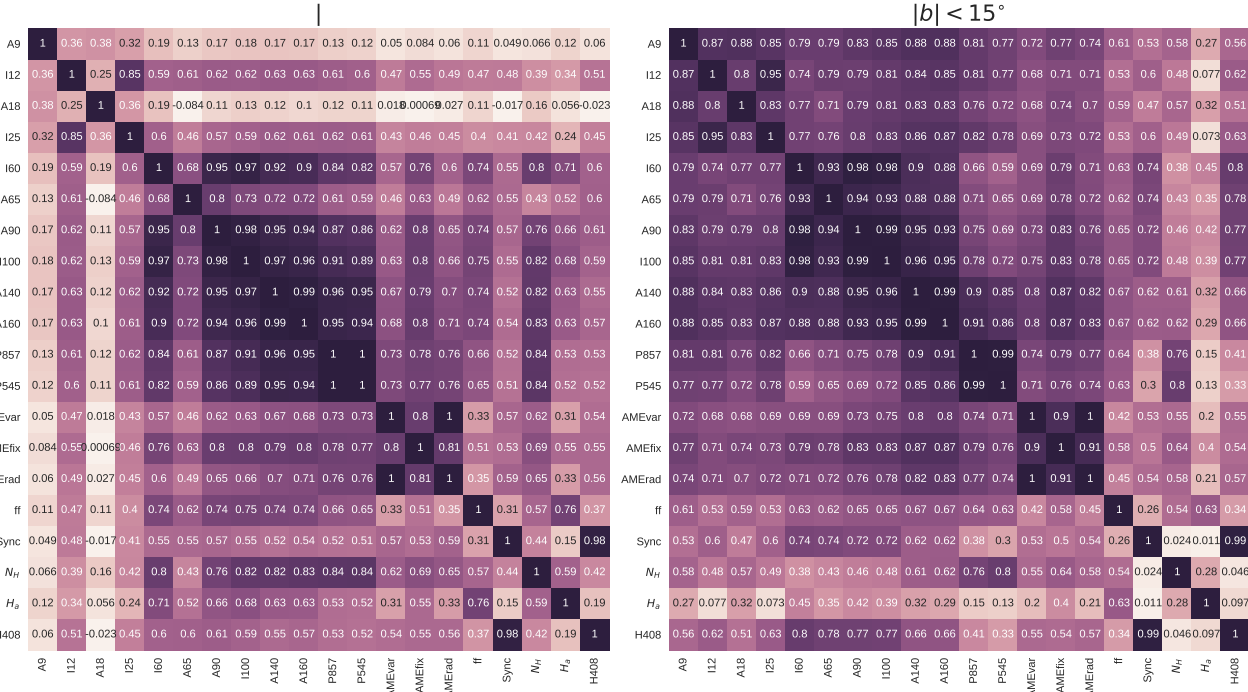


Figure 4.6: Cross-correlation (r_s) matrix for the IR intensities (unscaled) vs. each other, essentially the same comparison as in Fig. 4.2, except that the pixel mask is applied.

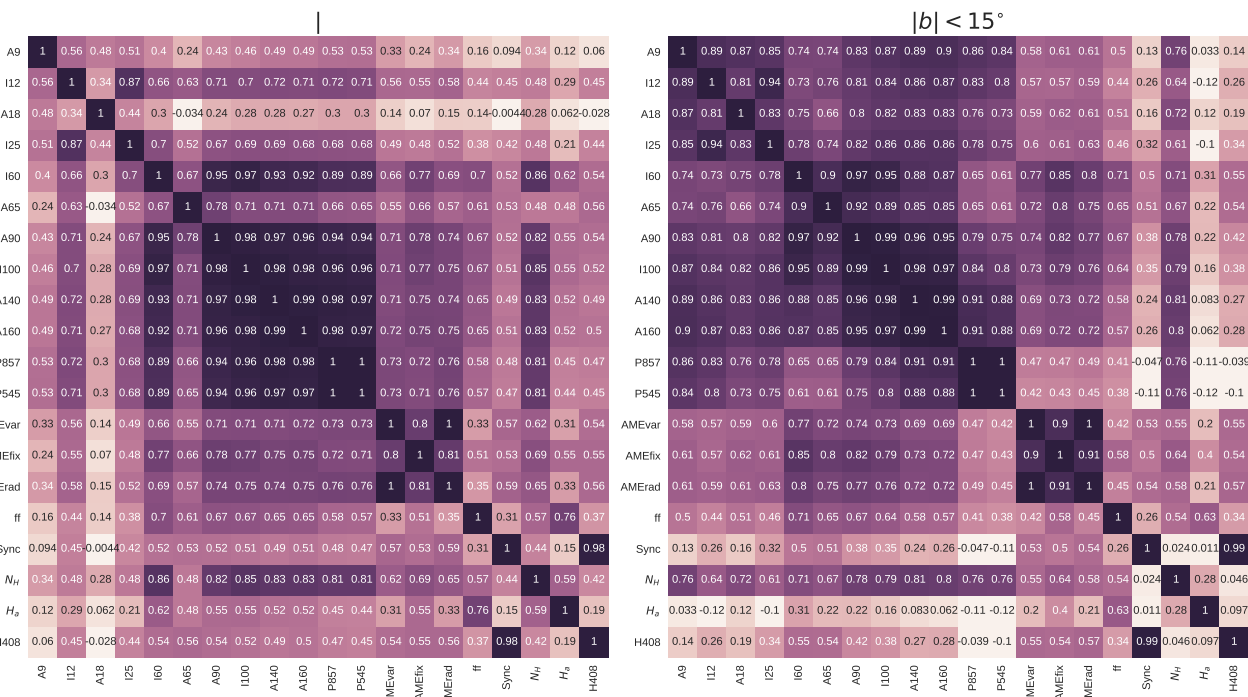


Figure 4.7: Cross-correlation (r_s) matrix for the U -normalized IR intensities vs. each other, and also against the AME components, other PC products, and ancillary data. Only the IR maps are divided by U -other data is unchanged from Fig. 4.6)

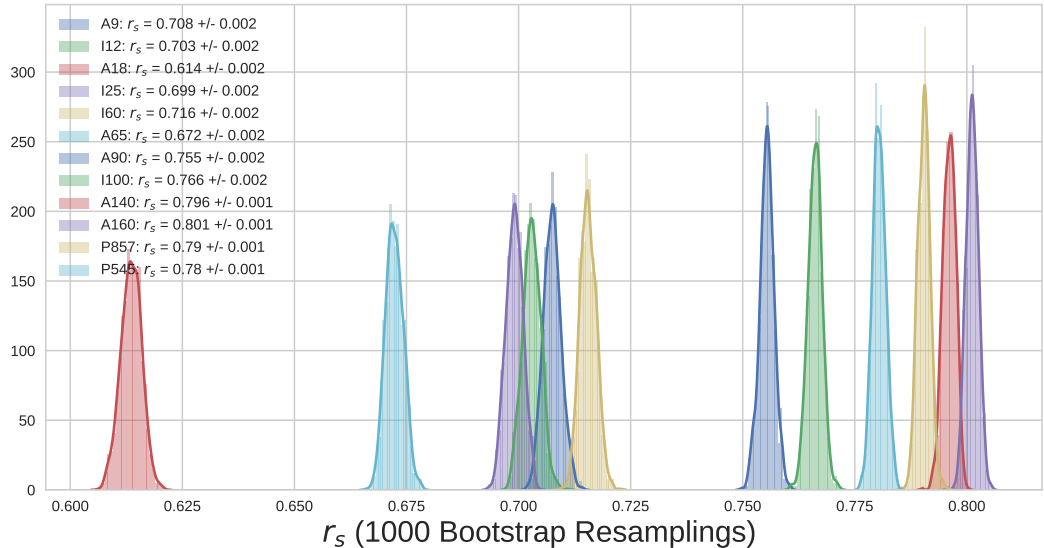


Figure 4.8: .

883 the computational challenges presented by a well-sampled bootstrap of all 700,000 pixels in the full
 884 sky. Because the mask applied here leaves us with approximately 1/7 of the sky, a bootstrap of N
 885 iterations with N pixels becomes tractable (though ideally we would prefer $n_{iterations} > n_{samples}$). We
 886 show the comparison only for the AME_{var} component also due to computational constraints. The r_s
 887 distributions for each IR band vs. AME are shown in Fig. 4.8

888 4.4 Spatial variation of correlations

889 To understand how these trends may vary across the sky, we produce an all-sky maps of r_s for AME
 890 vs. IR emission, without employing any pixel mask. From the NSIDE 256 input maps of AME and 4
 891 IR wavelength maps, we produce NSIDE 8 maps of r_s . These maps are shown in Figs. 4.9 and 4.10.

892

893 4.5 Discussion

894 4.5.1 AME:Dust

895 As noted in Ch. 1, previous studies found that the AME generally correlates at dust-related IR wave-
 896 lengths (Ysard et al. 2010; Planck Collaboration et al. 2014d; Hensley et al. 2016). We see the same
 897 overall pattern in the present study.

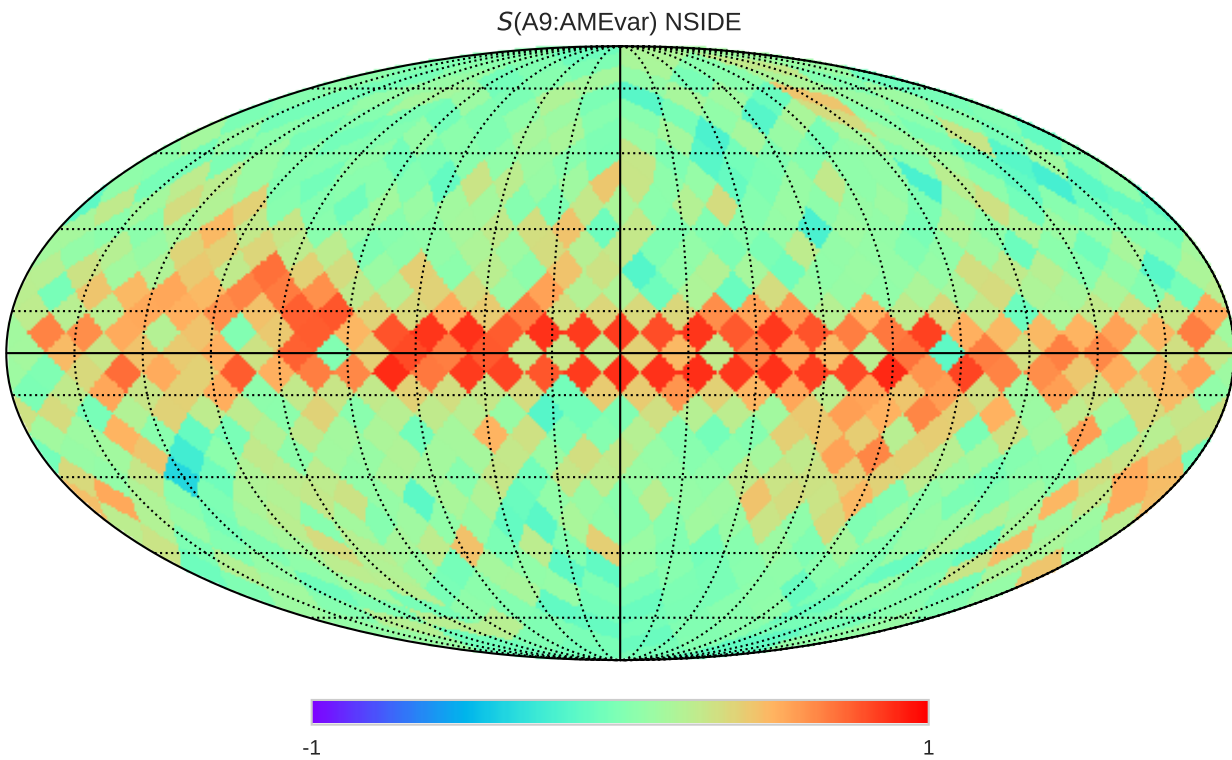


Figure 4.9: Spatial map of r_s between the AME and IR intensity for 4 bands: 9 μm , 12 μm , 25 μm , and 140 μm . r_s is calculated for all NSIDE 256 pixels within each NSIDE 8 pixel-sized bin.

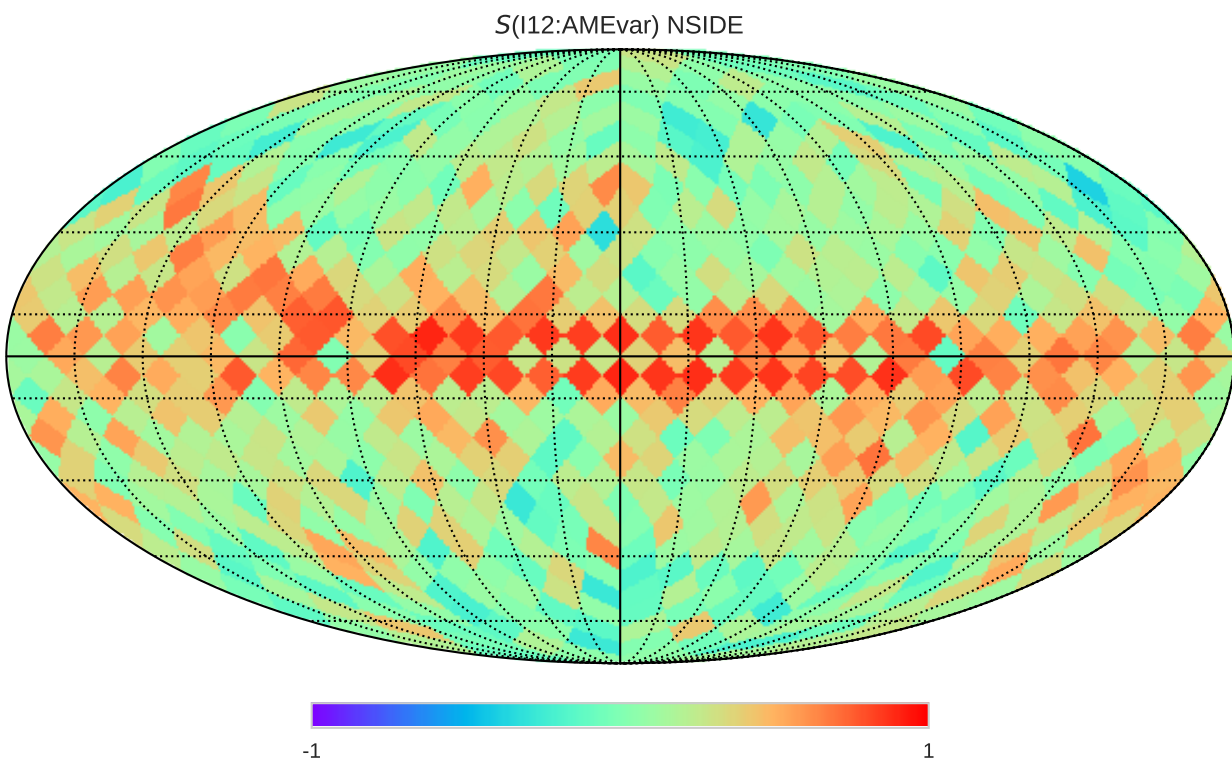


Figure 4.10

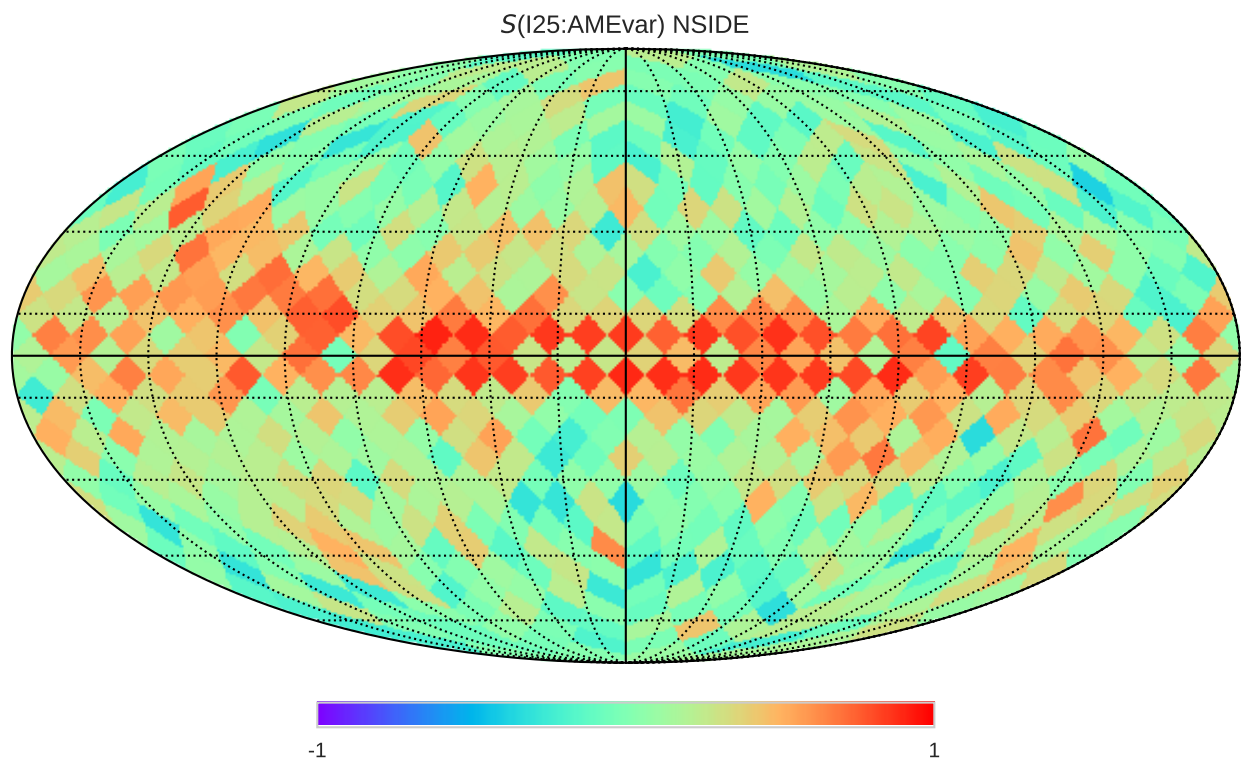


Figure 4.11

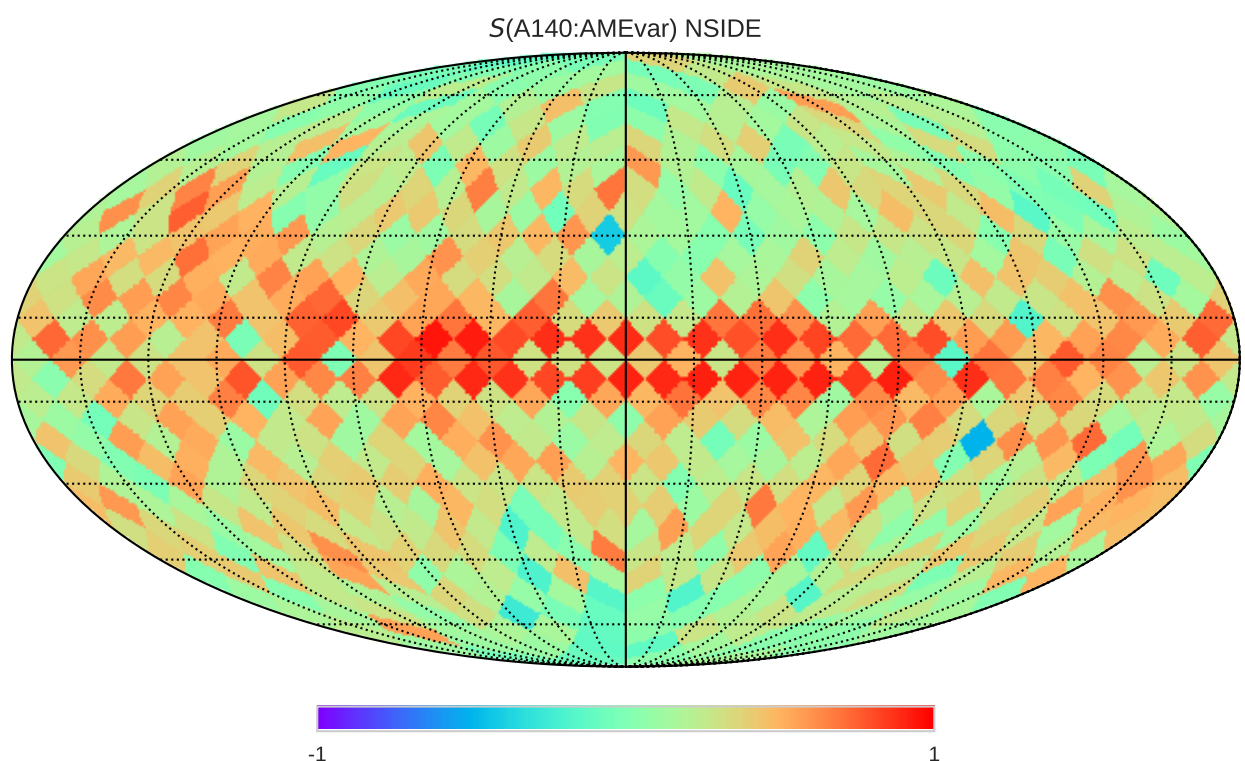


Figure 4.12

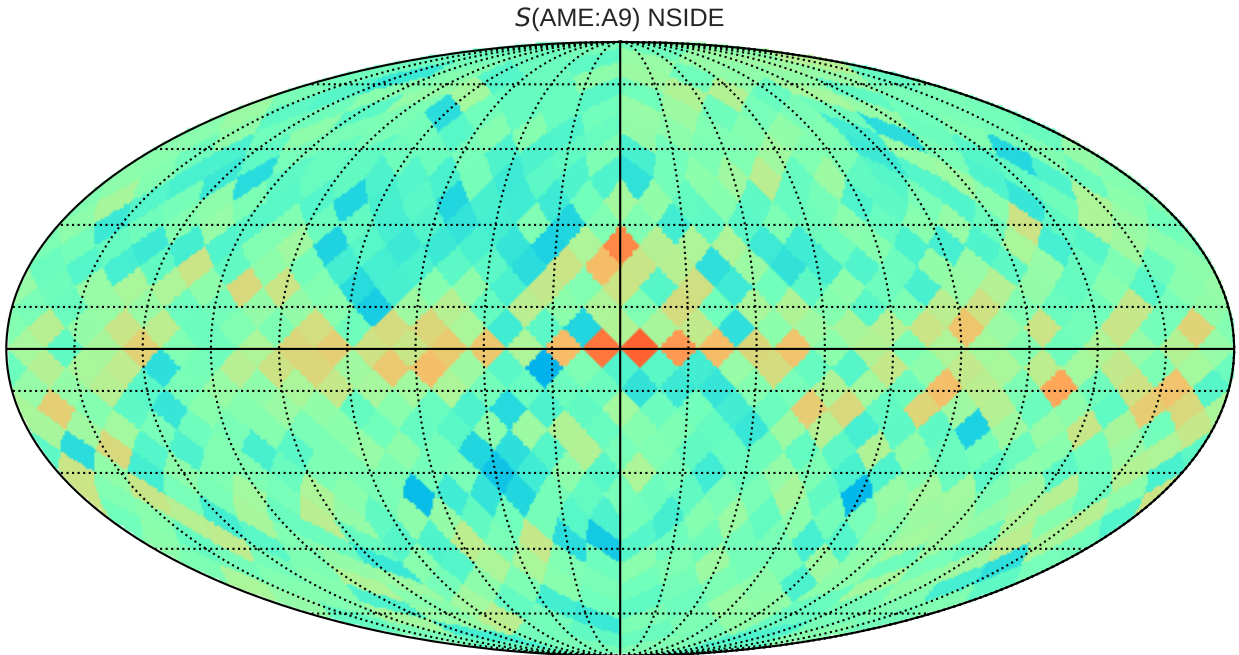


Figure 4.13: Spatial map of r_s between the AME and IR intensity as in Fig. ??, but with the AME and IR maps first normalized by dust radiance R .

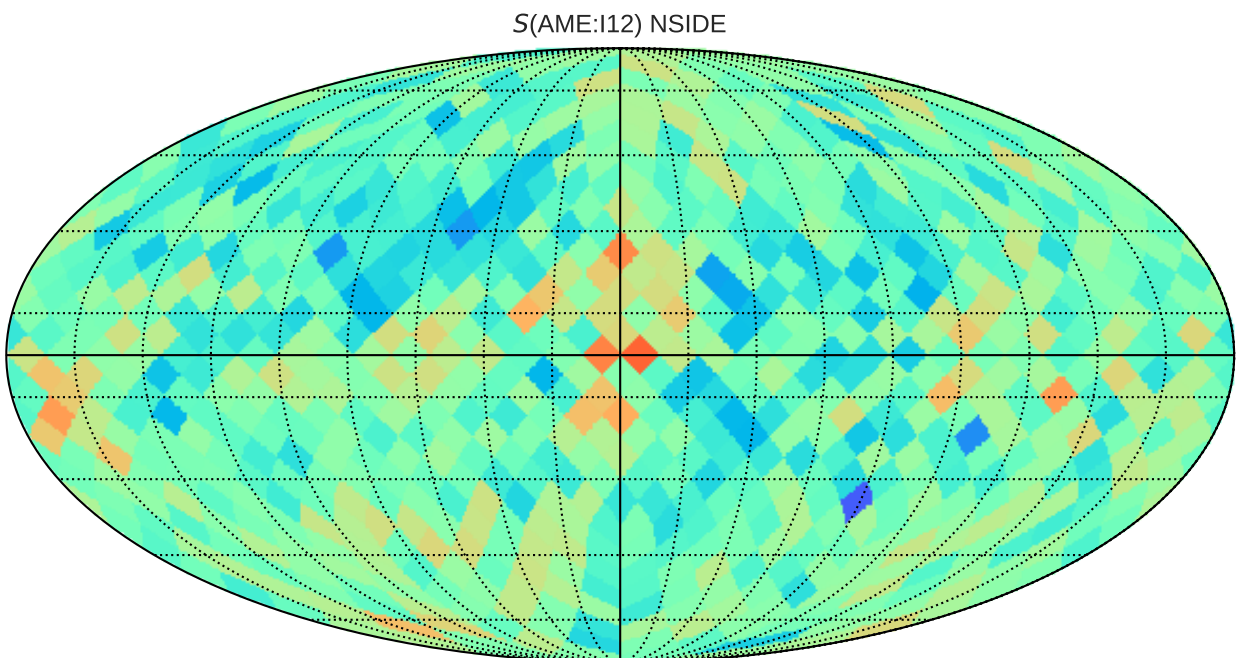


Figure 4.14

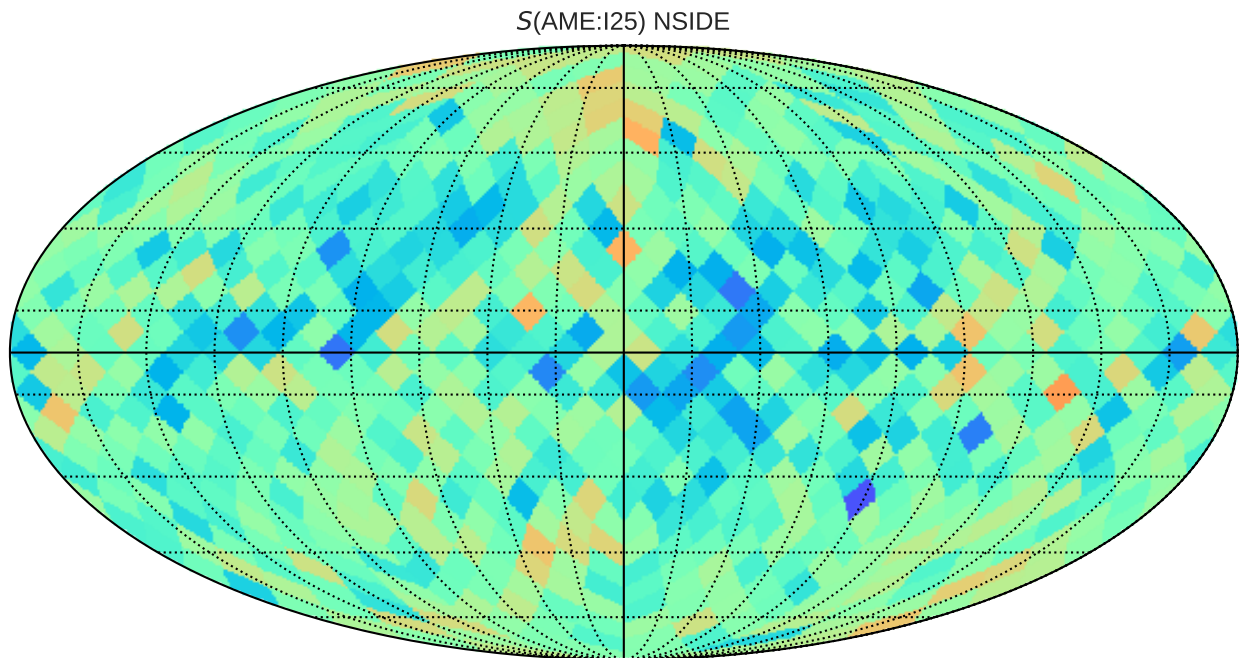


Figure 4.15

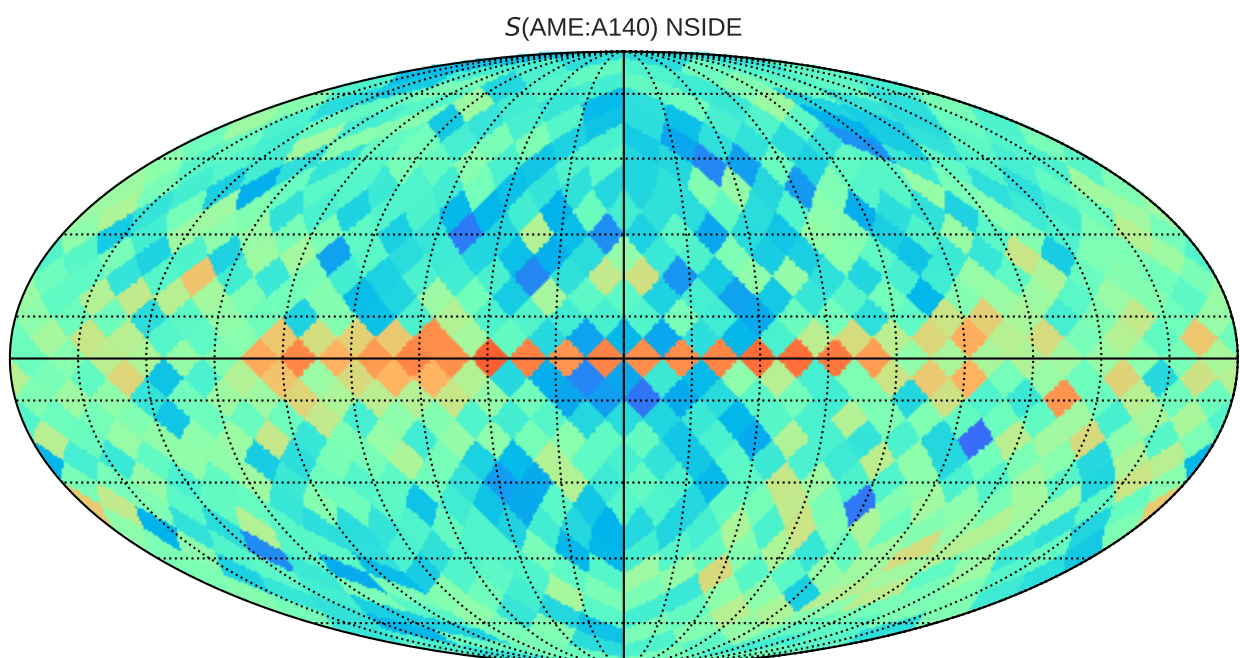


Figure 4.16

898 In our all-sky comparison, we find a first-order correlation between IR intensity and AME intensity,
899 for each of the 12 wavelengths sampled. This is again consistent with the previous investigations
900 of the AME cited above, in that the FIR emission shows the tightest correlation with the AME inten-
901 sity.

902 In testing for a second-order correlation, we divided the IR intensities and AME intensity by
903 the dust radiance, and again performed the band-by-band all-sky comparison. There is evidence of
904 a residual correlation between I_{MIR} and I_{AME}/R . Unsurprisingly, the strong correlation between
905 I_{FIR} and I_{AME} disappears when scaling by R , as the the FIR bands are dominated by thermal dust
906 emission. In this case, we again find no evidence of an improved correlation for the PAH-dominated
907 bands.

908 The closeness of the correlation coefficients found here is consistent with the results of the IRAS
909 vs. AME correlation test result from Planck Collaboration et al. (2014d). They found that the corre-
910 lation coefficient among the 4 IRAS bands (12, 25, 60, and 100 μm) differ from one another only by
911 about 5%, across the whole set of 98 regions. The trend of AKARI MIR and FIR data vs. the AME
912 does not disagree with their IRAS comparison. This work adds that bands longer than IRAS 100 μm
913 also correlate strongly with AME, especially the two Planck/HFI bands used.

914 4.5.2 AME:PAH

915 Each of the bands sampled show correlation with the AME, however the FIR bands always show the
916 strongest correlation. In fact, the correlation pattern of AME vs. each of the IR bands, very strongly
917 resembles the correlation results of the FIR vs. all of the other maps. This is readily apparent from
918 the pixel-density plots in Figs. 4.1 and 4.4, wherein the FIR bands pixels show a very similar density
919 profile vs. the AME. In attempting to factor out this first-order correlation, dividing the AME and IR
920 intensities by U for each pixel, we find the there is still a residual correlation between the MIR bands
921 and the AME.

922 4.5.3 AME: T, G_0

923 According to spinning dust theory outlined in Draine & Lazarian (1998a) and in subsequent works
924 by Ysard & Verstraete (2010), the AME profile and intensity will depend in part on the ISRF- but as
925 is well-stated in Hensley & Draine (2017), exactly how the ISRF will affect the AME SED is a more
926 complicated question. Absorbed starlight photons may be able to rotationally excite the carriers, but

927 if an enhanced ISRF leads to increased dust heating, then the increased IR emission can rotationally
928 de-excite the carriers. Moreover the ISRF affects not only the dust temperature but ionization of the
929 carriers.

930 **4.5.4 Microwave foreground component separation**

931 There are known degeneracies between the foreground parameters of the COMMANDER maps
932 (spinning-dust, and free-free, synchrotron components as described in Planck Collaboration et al.
933 (2016b).) This can be demonstrated by comparing the ratio map of the PCXV intensity to thermal
934 dust intensity.

⁹³⁵ A Note on Data Dimensionality

⁹³⁶ While we aim to demonstrate the application of high dimensionality in these studies, we do not wish
⁹³⁷ to mislead readers that we have assembled a 12-dimensional photometric dataset, simply because we
⁹³⁸ have 12 wavebands. This statement may seem nonsensical at first, but makes sense when we consider
⁹³⁹ the covariance of the data. Just from the outside, and our faithful belief that FIR dust emission looks
⁹⁴⁰ something like a blackbody, or modified blackbody, or at the very least we can agree that emission
⁹⁴¹ from dust in thermal equilibrium would produce some sort of peaked continuum emission spanning
⁹⁴² multiple photometric bands' width. If we agree on this point, then it follows naturally that said bands
⁹⁴³ would be highly correlated with one another. This means that the number of truly independent data
⁹⁴⁴ dimensions is not only lower than the number of bands used here, it is much lower.

⁹⁴⁵ Fig. 17 shows the % of variance in the data retained by the first n principal components. Principal
⁹⁴⁶ components are found essentially by first finding the covariance matrix of the input data, and then
⁹⁴⁷ diagonalizing this matrix- the eigenvectors will be the basis vectors of each principal component. The
⁹⁴⁸ eigenvalues will give the explained covariance per component. Applied in this manner, the compo-
⁹⁴⁹ nents may not necessarily have a clear physical interpretation, but from a data analytics perspective
⁹⁵⁰ we can at least assess the redundancies in our data. Thus from Fig. 17, and choosing an arbitrary
⁹⁵¹ covariance "acceptable loss" of 99%, our photometric data set steeply reduces to 3 dimensions. The
⁹⁵² first component contains 98% of the total variance.

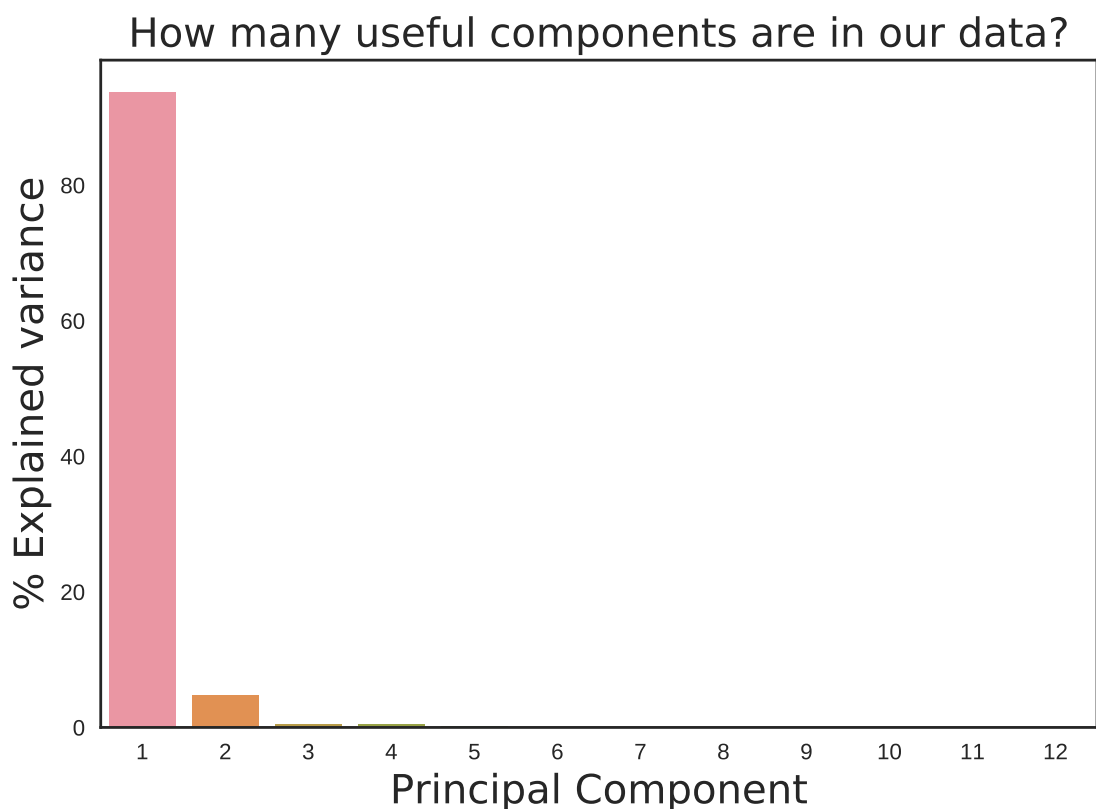


Figure 17: Explained variance decline for principal component analysis performed on a set of 12 all-sky infrared maps. The first three components account for over 99% of the total variance. The PCA fit is performed on the whole sky, after whitening the data, using the “scikitlearn”

953 This research made use of Montage. It is funded by the National Science Foundation under Grant
954 Number ACI-1440620, and was previously funded by the National Aeronautics and Space Admin-
955 istration's Earth Science Technology Office, Computation Technologies Project, under Cooperative
956 Agreement Number NCC5-626 between NASA and the California Institute of Technology

957 References

- 958 Ali-Haimoud, Y. 2010, SpDust/SpDust.2: Code to Calculate Spinning Dust Spectra, Astrophysics Source Code
959 Library
- 960 Ali-Haïmoud, Y. 2014, MNRAS, 437, 2728
- 961 Ali-Haïmoud, Y., Hirata, C. M., & Dickinson, C. 2009, MNRAS, 395, 1055
- 962 Allain, T., Leach, S., & Sedlmayr, E. 1996a, A&A, 305, 602
- 963 —. 1996b, A&A, 305, 616
- 964 Allamandola, L. J., Tielens, A. G. G. M., & Barker, J. R. 1985, ApJ, 290, L25
- 965 AMI Consortium et al. 2012, MNRAS, 423, 1463
- 966 Andrews, H., Boersma, C., Werner, M. W., Livingston, J., Allamandola, L. J., & Tielens, A. G. G. M. 2015,
967 ApJ, 807, 99
- 968 Aran, A. B. 2009, PhD thesis, UNIVERSIDAD AUTONOMA DE MADRID
- 969 Atwood, W. B., et al. 2009, ApJ, 697, 1071
- 970 Bennett, C. L., et al. 2003a, ApJS, 148, 97
- 971 —. 2003b, ApJS, 148, 1
- 972 BICEP2 Collaboration et al. 2014, Physical Review Letters, 112, 241101
- 973 Boggess, N. W., et al. 1992, ApJ, 397, 420
- 974 Bonnarel, F., et al. 2000, A&AS, 143, 33
- 975 Bot, C., Ysard, N., Paradis, D., Bernard, J. P., Lagache, G., Israel, F. P., & Wall, W. F. 2010, A&A, 523, A20
- 976 Boulanger, F., Baud, B., & van Albada, G. D. 1985, A&A, 144, L9
- 977 Compiègne, M., et al. 2011, A&A, 525, A103
- 978 Cunha, K., & Smith, V. V. 1996, A&A, 309, 892
- 979 Dale, D. A., Helou, G., Contursi, A., Silbermann, N. A., & Kolhatkar, S. 2001, ApJ, 549, 215
- 980 de Oliveira-Costa, A., Kogut, A., Devlin, M. J., Netterfield, C. B., Page, L. A., & Wollack, E. J. 1997, ApJ,
981 482, L17
- 982 de Oliveira-Costa, A., et al. 2002, ApJ, 567, 363
- 983 Dickinson, C., Paladini, R., & Verstraete, L. 2013, Advances in Astronomy, 2013, 1
- 984 Doi, Y., et al. 2015, PASJ, 67, 50
- 985 Draine, B. T. 2011, Physics of the Interstellar and Intergalactic Medium

REFERENCES

- 986 Draine, B. T., & Hensley, B. 2013, ApJ, 765, 159
- 987 Draine, B. T., & Lazarian, A. 1998a, ApJ, 494, L19
- 988 —. 1998b, ApJ, 508, 157
- 989 —. 1999, ApJ, 512, 740
- 990 Draine, B. T., & Li, A. 2001a, ApJ, 551, 807
- 991 —. 2001b, ApJ, 551, 807
- 992 —. 2007a, ApJ, 657, 810
- 993 —. 2007b, ApJ, 657, 810
- 994 Duerr, R., Imhoff, C. L., & Lada, C. J. 1982, ApJ, 261, 135
- 995 Dwek, E. 1986, ApJ, 302, 363
- 996 Dwek, E., et al. 1997, ApJ, 475, 565
- 997 Efron, B. 1979, Ann. Statist., 7, 1
- 998 Erickson, W. C. 1957, ApJ, 126, 480
- 999 Ferrara, A., & Dettmar, R.-J. 1994, ApJ, 427, 155
- 1000 Finkbeiner, D. P., Schlegel, D. J., Frank, C., & Heiles, C. 2002, ApJ, 566, 898
- 1001 Flauger, R., Hill, J. C., & Spergel, D. N. 2014, J. Cosmology Astropart. Phys., 8, 039
- 1002 Galliano, F., et al. 2011, A&A, 536, A88
- 1003 Giard, M., Lamarre, J. M., Pajot, F., & Serra, G. 1994, A&A, 286
- 1004 Gillett, F. C., Forrest, W. J., & Merrill, K. M. 1973, ApJ, 183, 87
- 1005 Gillett, F. C., Forrest, W. J., Merrill, K. M., Soifer, B. T., & Capps, R. W. 1975, ApJ, 200, 609
- 1006 Górski, K. M., Hivon, E., Banday, A. J., Wandelt, B. D., Hansen, F. K., Reinecke, M., & Bartelmann, M. 2005,
1007 ApJ, 622, 759
- 1008 Hanson, D., et al. 2013, Physical Review Letters, 111, 141301
- 1009 Haslam, C. G. T., Salter, C. J., Stoffel, H., & Wilson, W. E. 1982, A&AS, 47, 1
- 1010 Hensley, B. S., & Draine, B. T. 2017, ApJ, 836, 179
- 1011 Hensley, B. S., Draine, B. T., & Meisner, A. M. 2016, The Astrophysical Journal, 827, 45
- 1012 Hoang, T., Vinh, N.-A., & Quynh Lan, N. 2016, ApJ, 824, 18
- 1013 Hony, S., Van Kerckhoven, C., Peeters, E., Tielens, A. G. G. M., Hudgins, D. M., & Allamandola, L. J. 2001,
1014 A&A, 370, 1030
- 1015 Hoyle, F., & Wickramasinghe, N. C. 1970, Nature, 227, 473
- 1016 Ishihara, D., et al. 2007, PASJ, 59, S443
- 1017 —. 2010, A&A, 514, A1
- 1018 Israel, F. P., Wall, W. F., Raban, D., Reach, W. T., Bot, C., Oonk, J. B. R., Ysard, N., & Bernard, J. P. 2010,
1019 A&A, 519, A67

-
- 1020 Johnson, H. L. 1966, ARA&A, 4, 193
- 1021 Jones, A. P. 2009, A&A, 506, 797
- 1022 Jones, A. P., Fanciullo, L., Köhler, M., Verstraete, L., Guillet, V., Bocchio, M., & Ysard, N. 2013, A&A, 558, A62
- 1024 Jones, A. P., Köhler, M., Ysard, N., Bocchio, M., & Verstraete, L. 2017, A&A, 602, A46
- 1025 Kawada, M., et al. 2007a, PASJ, 59, S389
- 1026 —. 2007b, PASJ, 59, 389
- 1027 Kelsall, T., et al. 1998, ApJ, 508, 44
- 1028 Kessler, M. F., et al. 1996, A&A, 315, L27
- 1029 Koenig, X., Hillenbrand, L. A., Padgett, D. L., & DeFelippis, D. 2015, AJ, 150, 100
- 1030 Kogut, A., Banday, A. J., Bennett, C. L., Gorski, K. M., Hinshaw, G., & Reach, W. T. 1996, ApJ, 460, 1
- 1031 Kondo, T., et al. 2016, AJ, 151, 71
- 1032 Lau, R. M., Herter, T. L., Morris, M. R., Li, Z., & Adams, J. D. 2015, Science, 348, 413
- 1033 Leach, S. M., et al. 2008, A&A, 491, 597
- 1034 Leitch, E. M., Readhead, A. C. S., Pearson, T. J., & Myers, S. T. 1997, ApJ, 486, L23
- 1035 Li, A., & Draine, B. T. 2001, ApJ, 554, 778
- 1036 Lovas, F. J., McMahon, R. J., Grabow, J.-U., Schnell, M., Mack, J., Scott, L. T., & Kuczkowski, R. L. 2005, Journal of the American Chemical Society, 127, 4345, pMID: 15783216
- 1038 Maddalena, R. J. 1986, PhD thesis, National Aeronautics and Space Administration. Goddard Inst. for Space Studies, New York, NY.
- 1039
- 1040 Maddalena, R. J., & Morris, M. 1987, ApJ, 323, 179
- 1041 Martin, D. C., et al. 2005, ApJ, 619, L1
- 1042 Mathis, J. S., Mezger, P. G., & Panagia, N. 1983, A&A, 128, 212
- 1043 Mathis, J. S., Rumpl, W., & Nordsieck, K. H. 1977, ApJ, 217, 425
- 1044 Mattila, K., Lemke, D., Haikala, L. K., Laureijs, R. J., Leger, A., Lehtinen, K., Leinert, C., & Mezger, P. G. 1996, A&A, 315, L353
- 1046 Merrill, K. M., Soifer, B. T., & Russell, R. W. 1975, ApJ, 200, L37
- 1047 Miville-Deschénes, M.-A., & Lagache, G. 2005, ApJS, 157, 302
- 1048 Murakami, H., et al. 1996, PASJ, 48, L41
- 1049 —. 2007, PASJ, 59, 369
- 1050 Murdin, P., & Penston, M. V. 1977, MNRAS, 181, 657
- 1051 Neugebauer, G., et al. 1984, ApJ, 278, L1
- 1052 Ochsendorf, B. B., Brown, A. G. A., Bally, J., & Tielens, A. G. G. M. 2015, ApJ, 808, 111
- 1053 Onaka, T. 2000, Advances in Space Research, 25, 2167

REFERENCES

- 1054 Onaka, T., Mizutani, M., Tomono, D., Shibai, H., Nakagawa, T., & Doi, Y. 1999, in ESA Special Publication,
1055 Vol. 427, *The Universe as Seen by ISO*, ed. P. Cox & M. Kessler, 731
- 1056 Onaka, T., Yamamura, I., Tanabe, T., Roellig, T. L., & Yuen, L. 1996, PASJ, 48, L59
- 1057 Onaka, T., et al. 2007, PASJ, 59, 401
- 1058 Ootsubo, T., et al. 2016, PASJ, 68, 35
- 1059 Paladini, R., Ingallinera, A., Aglizzo, C., Tibbs, C. T., Noriega-Crespo, A., Umana, G., Dickinson, C., &
1060 Trigilio, C. 2015, ApJ, 813, 24
- 1061 Pavlyuchenkov, Y. N., Kirsanova, M. S., & Wiebe, D. S. 2013, Astronomy Reports, 57, 573
- 1062 Perrott, Y. C., et al. 2018, MNRAS, 473, 1157
- 1063 Pettit, E., & Nicholson, S. B. 1922, ApJ, 56, 295
- 1064 —. 1928, ApJ, 68
- 1065 Pilleri, P., Montillaud, J., Berné, O., & Joblin, C. 2012, A&A, 542, A69
- 1066 Planck Collaboration et al. 2011a, A&A, 536, A1
- 1067 —. 2011b, A&A, 536, A20
- 1068 —. 2014a, A&A, 571, A1
- 1069 —. 2014b, A&A, 571, A8
- 1070 —. 2014c, A&A, 571, A12
- 1071 —. 2014d, A&A, 565, A103
- 1072 —. 2016a, A&A, 594, A1
- 1073 —. 2016b, A&A, 594, A10
- 1074 —. 2016c, A&A, 594, A25
- 1075 —. 2016d, A&A, 586, A132
- 1076 —. 2017, A&A, 599, A51
- 1077 Puget, J. L., Leger, A., & Boulanger, F. 1985, A&A, 142, L19
- 1078 Purcell, E. M. 1976, ApJ, 206, 685
- 1079 Reynolds, R. J., Tufte, S. L., Haffner, L. M., Jaehnig, K., & Percival, J. W. 1998, PASA, 15, 14
- 1080 Russell, R. W., Soifer, B. T., & Willner, S. P. 1977, ApJ, 217, L149
- 1081 Sakata, A., Wada, S., Tanabe, T., & Onaka, T. 1984, ApJ, 287, L51
- 1082 Sellgren, K. 1984, ApJ, 277, 623
- 1083 Sellgren, K., Werner, M. W., & Dinerstein, H. L. 1983, ApJ, 271, L13
- 1084 Sheehy, C., & Slosar, A. 2017, ArXiv e-prints
- 1085 Skrutskie, M. F., et al. 2006, AJ, 131, 1163
- 1086 Sodroski, T. J., Dwek, E., Hauser, M. G., & Kerr, F. J. 1987, ApJ, 322, 101

-
- 1087 Sodroski, T. J., et al. 1994, ApJ, 428, 638
- 1088 Takita, S., et al. 2015, PASJ, 67, 51
- 1089 Thorwirth, S., Theulé, P., Gottlieb, C. A., McCarthy, M. C., & Thaddeus, P. 2007, ApJ, 662, 1309
- 1090 Tibbs, C. T., et al. 2011, MNRAS, 418, 1889
- 1091 Truemper, J. 1982, 2, 241
- 1092 von Hausegger, S., & Liu, H. 2015, J. Cosmology Astropart. Phys., 8, 029
- 1093 Weingartner, J. C., & Draine, B. T. 2001, ApJ, 548, 296
- 1094 Werner, M. W., et al. 2004, ApJS, 154, 1
- 1095 Wright, E. L., et al. 2010, AJ, 140, 1868
- 1096 Young, E. T., et al. 2012, ApJ, 749, L17
- 1097 Ysard, N., Juvela, M., & Verstraete, L. 2011, A&A, 535, A89
- 1098 Ysard, N., Miville-Deschénes, M. A., & Verstraete, L. 2010, A&A, 509, L1
- 1099 Ysard, N., & Verstraete, L. 2010, A&A, 509, A12